Predicting the Anomalous Density of a Dense Fluid Confined Within a Carbon Nanotube

by

Gerald J. Wang

B.S. Mechanical Engineering and B.S. Mathematics & Physics
Yale University (2013)

Submitted to the Department of Mechanical Engineering
in partial fulfillment of the requirements for the degree of

Master of Science in Mechanical Engineering

at the

MASSACHUSETTS INSTITUTE OF TECHNOLOGY

June 2015

Author ..... Signature redacted
Department of Mechanical Engineering
May 19, 2015

Certified by ..... Signature redacted
Nicolas G. Hadjiconstantinou
Professor of Mechanical Engineering
Thesis Supervisor

Accepted by ..... Signature redacted
David E. Hardt
Chairman, Department Committee on Graduate Theses

Predicting the Anomalous Density of a Dense Fluid Confined Within a Carbon Nanotube

by

Gerald J. Wang

Submitted to the Department of Mechanical Engineering
on May 19, 2015, in partial fulfillment of the
requirements for the degree of
Master of Science in Mechanical Engineering

Abstract

The equilibrium density of fluids under nanoconfinement can differ substantially from their bulk density. Using a mean-field approach to describe the energetic landscape near the carbon nanotube (CNT) wall, we obtain analytical results describing the lengthscales associated with the layering observed at the interface of a Lennard-Jones fluid and a CNT. We also show that this approach can be extended to describe the multiple-ring structure observed in larger CNTs. When combined with molecular simulation results for fluid density in the first two rings, this approach allows us to derive a closed-form prediction for the overall equilibrium fluid density as a function of CNT radius that is in excellent agreement with molecular dynamics simulations. We also show how aspects of this theory can be extended to describe some features of water confinement within CNTs and find good agreement with results from the literature. Finally, we present evidence that this model for anomalous fluid density can also be applied to understand simple nanoscale flow phenomena.

Thesis Supervisor: Nicolas G. Hadjiconstantinou
Title: Professor of Mechanical Engineering

Acknowledgments

"It takes a village to raise a child... and even more if that child doesn't already have previous experience with molecular dynamics."

– Anybody who has ever done molecular dynamics

In the spirit of this great folk saying (or perhaps folk-saying-to-be), there are many (many) people who have helped me become who I am today. I am greatly indebted to all of them for their generosity and support; the thermodynamic limit of infinite gratitude does not begin to capture my feelings for all of these remarkable individuals (and government/corporate entities). What follows is, to me, the most cherished and celebrated of the \begin{enumerate}'s in this document. I would like to thank...

1. Prof. Nicolas Hadjiconstantinou. His unparalleled guidance, coupled to infinite reservoirs of knowledge, humor, and patience, has defined my research experience at MIT. I can only hope that over the next several years, I might take even infinitesimal steps toward equilibration with these astonishing baths.

2. The Department of Energy Computational Science Graduate Fellowship, the Tau Beta Pi Graduate Fellowship, and Aramco Services Company. I am very grateful to all of them for their generous support of my research endeavors.

3. Prof. Sarah Demers and Prof. Nicholas Ouellette. Their mentorship and support have been the basis of so much of my scientific identity. Though their research groups work at very different lengthscales, I am very proud to have been a part of both. I am thrilled that my current research has struck a balance by operating near the (geometric) average of their respective lengthscales.

4. Rachel Kurchin and Nickolas Demas. On a day-to-day basis, they are two of my greatest *raisons d'être.* Admittedly, there are many such *raisons* (cf. raisins), but Nick and Rachel in particular are exceptional for their charm, cheer, compassion, and camaraderie – simply unmatched by any grape, dried or otherwise. I am endlessly grateful to both.

5. Michael Boutilier, Nisha Chandramoorthy, Margaux Filippi, Mojtaba Forghani, Ashkan Hosseinloo, Dr. Hussain Karimi, Dr. Colin Landon, Hung Nguyen, J.-P. Peraud, and Mathew Swisher. Their wit, intelligence, thoughtfulness, and overall incomparable company have made me proud to call the Nexus my home away from home (away from home (away from home)).

6. Deborah Alibrandi, Joan Kravit, and Leslie Regan. Underneath their bright smiles and constant enthusiasm, it can be easy to lose sight of the steel-trap minds that routinely solve problems with many more degrees of freedom than any system proposed in this thesis.

7. Rick Herron, Dr. Nancy Shedd, and Dr. Alexander Kurchin. Their cardiovascular prowess and unrelenting keenness on athletic tourism have spared me from the most pernicious vicissitudes of a theorist's oft-too-sedentary lifestyle.

8. Prof. David J. Griffiths. He is the *sine qua non* of my physics education as well as my insatiable *thirst* for *italics*.

9. a) Tong Zhan. He is someone with whom laughs flow as freely as nanoscale fluids (Tong, that means you have to read this thesis now). Unrelatedly, his friendship is the single most valuable asset in my 401k portfolio to date.

   b) Henry Wilkin. Without his friendship, I would be grievously ignorant about the Inverse Function Theorem, Manos: The Hands of Fate, bees, anyonic spin statistics, and Adventure Time, all of which might have played key roles in Chapter 8 of this thesis if such a chapter existed.

   c) Jenna Freudenburg. Without her careful logic and firm convictions, I might never have come to accept the divinity of Higher Beings, like John Urschel.

10. Last, and most of all, my wonderful family – my father Jie, my mother Hong, my sister Jennie, the cat Simba, and countless others. I owe everything that I am to them (minus the cat).

Contents

List of Figures

List of Tables

Chapter 1

Introduction

"My density has brought me to you!"

– George McFly in *Back to the Future*

1.1 Through the Nano-Looking Glass

The behavior of fluids at the nanoscale can differ dramatically from their familiar behavior at the macroscale. Whereas classical fluids can be studied using macroscopic balance laws – to wit, the Navier-Stokes equations – the properties of *nanoconfined fluids* (i.e. a confined fluid with a confinement lengthscale that is comparable to the fluid molecular lengthscale) are often dominated by *molecular-scale features.*

Fluids under nanoscale confinement exhibit many remarkable properties. For example, one phenomenon that has garnered considerable attention over the last decade is the tendency for fluids to flow through carbon nanotubes (CNTs) at rates that are substantially higher than those dictated by macroscale fluid mechanics. In particular, it has been observed in both experiments and computer simulations that for water flowing through a CNT, this flow-rate enhancement can be up to four orders of magnitude [11, 12, 13, 14]. There is clear evidence that fluids at the nanoscale are governed by a different fundamental physics than classical fluids, and that there is great engineering potential for nanofluidics.

1.2 The Anomalous Density Phenomenon

In this thesis, we present new analytical and computational insights on yet another nanofluidic phenomenon: the *anomalous density*. When a fluid is placed under nanoconfinement (e.g. within a CNT) and this nanoconfined system is in equilibrium with a large fluid bath, then the density (defined in the usual sense as total mass of confined fluid molecules normalized by available volume) of the nanoconfined fluid can differ dramatically from the density of the bulk fluid. In particular, the nanoconfined density is generally *lower* than the bulk density – for water confined within a CNT, this value can be as low as 200 kg m^{-3} [1].

The qualitative relationship between the anomalous density of water and confinement lengthscale (in this case, the radius of the confining CNT) can be observed in Figure 1-1, from [1]. This figure shows that for large CNT radii, the water density approaches the familiar bulk value of 1000 kg m^{-3}; on the other hand, fluid density falls dramatically as the confinement lengthscale decreases.

1.3 Applications of the Anomalous Density

Understanding and predicting this anomaly is very important for a variety of nanoscale applications. For example, in the area of public health, Hinds *et al.* propose several potential designs for CNT-based desalination devices [15]. The possibility of drug delivery across cell membranes has been studied by Park *et al.* [16]. In both cases, estimating efficiency and calibrating fluid throughput would in part depend on the amount of fluid that can fit within each nanoconfining geometry.

On the energy frontier, developing a model for anomalous density can assist in calculations of the shale gas or oil content of nanoporous rock [17]. Such a model could also play a role in designing and optimizing nano-osmotic energy harvesters that use boron-nitride nanotubes [18].

From a fundamental physics perspective, an understanding of the anomalous density could also potentially assist with the development of sub-continuum models that

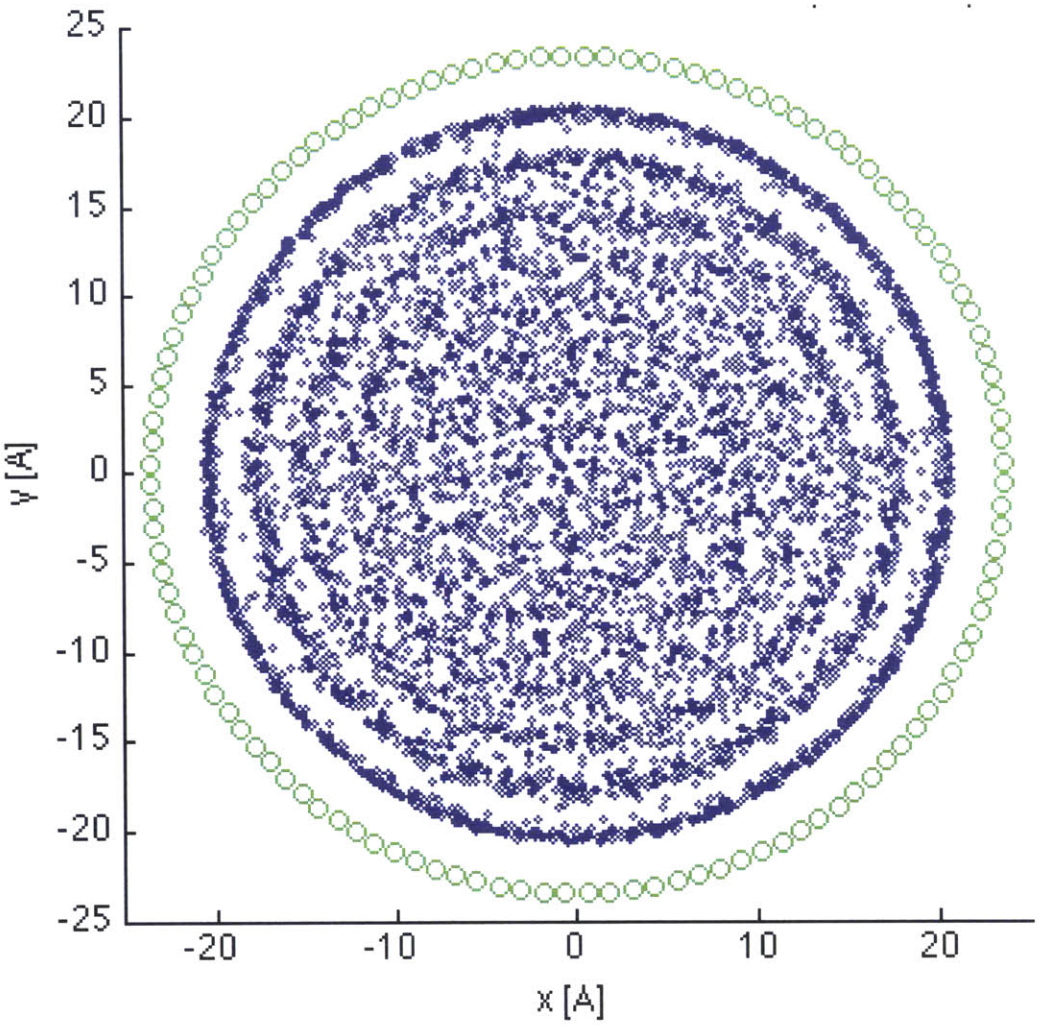

Figure 1-2: Cross-sectional view of equilibrium LJ fluid structure within a CNT ($R = 23.5\mathring{A}$), obtained from MD simulation. Green circles denote wall carbon atoms and blue dots denote fluid atoms.

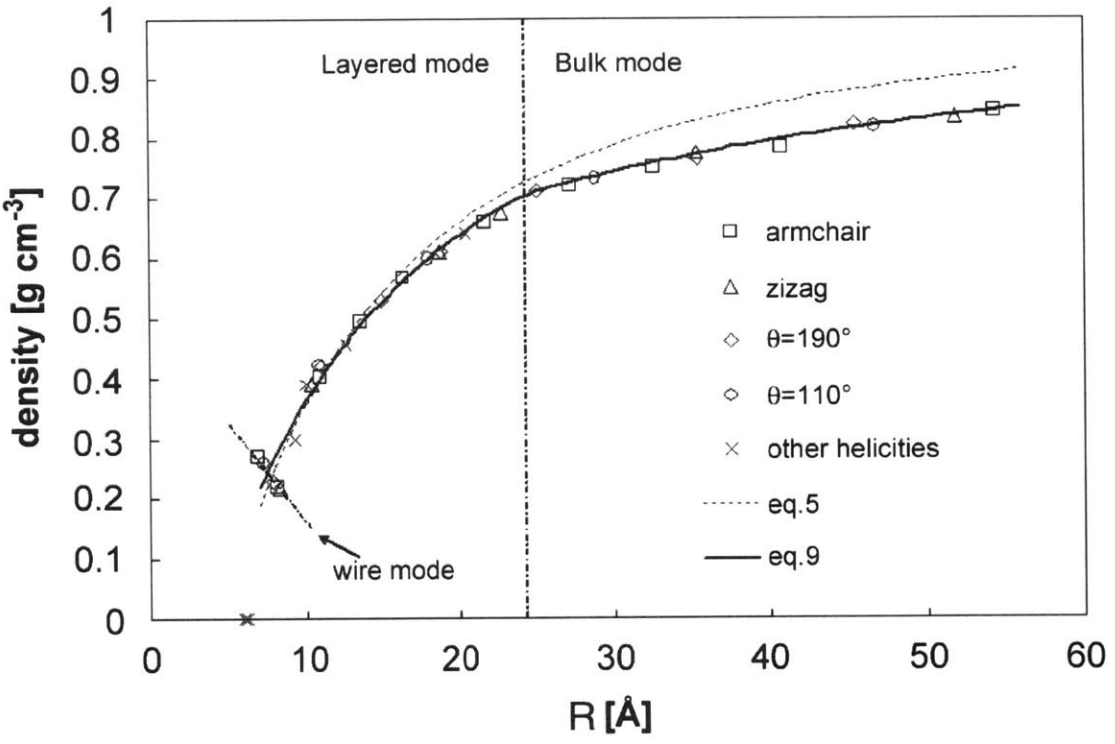

Figure 1-1: Relationship between anomalous water density and confinement length-scale (in this case, R, the radius of the confining CNT), from [1]. The data points were obtained through molecular dynamics simulations; Eqns. 5 and 9 in the legend refer to empirical fits for the simulation data used in [1].

predict anomalous fluid flow rates through CNTs. This could be accomplished using theories that posit direct relationships between anomalous flow and density depletions [19, 20] as well as theories that indirectly rely upon the equilibrium fluid density (e.g. a theory that relates fluid kinetics to excess entropy, which in turn depends on the equilibrium fluid density [21]).

Predicting equilibrium densities under confinement can also be very beneficial from a computational point of view, because it allows realistic simulation of nanofluidic systems without coupling to an external fluid bath, which is often very computationally expensive [5, 22, 23]. Benefits are possible even when a fluid bath is included in such systems. For example, it is common to pre-fill nanopores with fluid molecules to reduce equilibration time; knowledge of the *correct* equilibrium density minimizes the computational cost associated with equilibration.

1.4 Prior Work

Previous work has investigated these anomalous equilibrium densities under nanoconfinement, primarily using molecular dynamics simulations. In particular, there have been many studies of the equilibrium behavior of Lennard-Jones fluids under nanoconfinement. Travis and Gubbins have studied the structure of Lennard-Jones fluids within slit pores [24], whereas Wu *et al.* and Liu *et al.* have investigated the structure of these fluids within CNTs [7, 22]. Using Monte Carlo simulation, Shai *et al.* have studied the structure and heat capacity of neon and xenon (two fluids very accurately described by the Lennard-Jones potential) within a CNT environment [25].

There have also been many equilibrium studies of nanoconfined water. Alexiadis and Kassinos have conducted a comprehensive study of the relationship between CNT radius and the anomalous density of water confined within the CNT, including the effects of CNT chirality [1] and the effects of using different molecular models for water or different CNT rigidities [26]. Similar problems have been studied by Wang, Zhu, Zhou, and Lu, who focused on the relationship between CNT structure and the hydrogen-bonding network of water molecules within the CNT [6]. Koga *et al.* have

investigated phase transitions and the possible existence of a solid-liquid critical point for water in a CNT [27]. The orientational distribution of water molecules within a CNT, and the effect of an external electric field on this distribution, has been studied extensively by Su and Guo [28].

These studies have established that fluids confined within a sufficiently large CNT will form concentric rings, or fluid layers, near the CNT wall [1, 6, 7, 22]. Near the center of the CNT, the fluid will exhibit little ordering and resemble bulk fluid, or fluid that is not "aware" of the presence of the CNT wall. These features can be seen in Fig. 1-2, which shows the equilibrium structure of a Lennard-Jones fluid in a CNT of radius 23.5$\mathring{A}$, obtained through molecular dynamics simulation. Numerous studies [8, 10, 24, 29] have observed the presence of a stand-off distance between the CNT wall and the fluid, determined empirically to be on the order of one atomic diameter.

Despite the large number of studies on equilibrium nanoconfined fluid structure, there is to date no first-principles model that can predict the lengthscales associated with the nanoscale fluid layering described above. Similarly, there is currently no method for predicting the magnitude of the anomalous density without the high computational costs of a density-functional theory calculation [30, 31].

1.5 Scope of Current Work

In this thesis, we present several new theoretical and computational results on fluids confined within CNTs. We begin in Chapter 2 by outlining the fundamentals of molecular dynamics (MD) simulation, a technique used extensively to support the models we build. We also discuss several interatomic potentials of interest in our work – most notably, the Lennard-Jones potential. In Chapter 3, we present a classical mean-field energetics argument, which allows us to develop analytical results on lengthscales of interest for nanoconfined fluids. Specifically, we predict the equilibrium locations and widths of nanoconfined fluid rings that form within CNTs. These lengthscales play an important role in understanding the anomalous density phenomenon. Chapter 4 provides a detailed description of the MD simulations performed, including simulation

settings and post-processing of simulation output. We present the results of these MD simulations in Chapter 5. In particular, we find excellent agreement between theory and simulation over a broad range of simulation conditions for Lennard-Jones fluids. We also show that key aspects of our theory can be extended to describe water confined within a CNT. Moreover, we demonstrate that these models can shed light on simple nanoscale flow phenomena. We conclude in Chapter 6 by summarizing the key contributions of this thesis and offering perspectives on future directions for this work.

Chapter 2

Fundamentals of Molecular Dynamics (MD) Simulations

"If you could stop every atom in its position and direction, and if your mind could comprehend all the actions thus suspended, then if you were really, really good at algebra you could write the formula for all the future...."

– Thomasina Coverly in *Arcadia*

Statistical physics is a powerful toolbox for analyzing nanoscale systems. However, when the number of degrees of freedom in the system becomes large (and the system Hamiltonian grows correspondingly unsightly), analytical approaches are often intractable. For example, the statistical properties of a dense nanofluid could in principle be obtained through analytical (or numerical) solution of the BBGKY hierarchy of equations [32, 33], but for real-world systems this is rarely practical. This motivates the need for a computational approach that can generate a large number of system microstates, amenable to statistical sampling. Toward this end, molecular dynamics is a particularly popular and successful simulation technique. MD deterministically generates the *time evolution* of a system using information about atomistic kinematics and interatomic potentials. This is accomplished by numerically integrating Newton's equations of motion for each constituent atom.

MD has been the simulation tool of choice for numerous investigations of nanoconfined fluid structure. In particular, MD has been used extensively in studies focused on LJ fluids [22, 23, 34], as well as studies focused on water [1, 9, 29, 35]. MD has also

been used to examine the effects of a wealth of simulation parameters on fluid structure, including temperature [36], presence of ions [37], and many choices of confining material [38, 39].

In this chapter, we present the fundamentals of the MD simulation technique. We begin by describing the basic MD algorithm, including the calculation of interatomic forces, the updating of atomic positions using knowledge of these forces, and the implementation of thermostats i.e. the maintenance of constant temperature in a simulation. We then discuss the interatomic potentials of interest in our work – namely, the LJ potential and various models for water. We conclude with a discussion of how thermodynamic properties are sampled from molecular trajectories obtained through MD simulation.

2.1 The Basic MD Algorithm

2.1.1 Time-Integration of Newton's Laws

The goal of MD simulation is to use knowledge about atomic positions and velocities, along with information about interatomic interactions, to predict positions and velocities in the future. This is done through time-integration of Newton's laws of motion. In particular, consider an atom of mass m_i located at position $\vec{r}_i$, where the potential field is $U = U(\vec{r}_i)$. Then this atom obeys the equation of motion:

$$m_i \frac{d^2\vec{r}_i}{dt^2} = -\frac{\partial U}{\partial \vec{r}_i} = \vec{f}_i \tag{2.1}$$

Here, $\vec{f}_i$ is of course the force exerted on this atom. Note that in this thesis, we will only consider *pair potentials* i.e. the potential field is uniquely determined by pairwise interactions between all atoms within the system. There are more-complex potentials (e.g. the Stillinger-Weber potential for silicon [40]) where configurations of triplets (or even more particles) also contribute to the system energy, but these are not needed to study the fluids of interest here.

Given a system of N interacting atoms, Eqn. (2.1) represents N coupled non-linear

ODEs, which unsurprisingly cannot be solved analytically for non-trivial systems i.e. $N > 2$. Thus we must use a numerical integration technique to update the $6N$ values of atomic positions and velocities.

2.1.2 Velocity Verlet

Using knowledge of $\vec{r}_i$ at time t (and all previous times), we can calculate the value of position at a time δt later, $\vec{r}_i(t+\delta t)$, as:

$$\vec{r}_i(t+\delta t) = \vec{r}_i(t) + \vec{v}_i(t)\delta t + \frac{1}{2}\vec{a}_i(t)\delta t^2 \tag{2.2}$$

where $\vec{a}_i = \vec{f}_i/m_i$. Analogously, we can update the velocity $\vec{u}_i$ using:

$$\vec{u}_i(t+\delta t) = \vec{u}_i(t) + \frac{\vec{a}_i(t) + \vec{a}_i(t+\delta t)}{2}\delta t \tag{2.3}$$

This approach is known as the *velocity Verlet algorithm* [41, 42]. This algorithm is the standard basis for numerical time integration in the molecular dynamics code LAMMPS [43] used in this thesis. We note several important aspects of the velocity Verlet algorithm:

1. This method is *self starting* and *explicit*. In other words, given initial positions and velocities (and interatomic potentials), we are immediately able to implement Eqns. (2.2) and (2.3) without specifying additional initial conditions. Moreover, at every timestep, we are able to calculate the LHS using known values for RHS quantities.

2. Velocity Verlet is a *symplectic integrator*. This means that as long as the forces in the system are conservative, the system Hamiltonian will not deviate substantially from its initial value in the long-time limit; in fact, the Hamiltonian will oscillate around its initial value.

3. The global errors in position and velocity are both $\mathcal{O}(\delta t^2)$.

4. For δt small, there is the possibility that $\delta t^2 \vec{a}(t)$ will be so small in magnitude that it gets lost in rounding errors.

The weakness discussed in the last item can be mitigated by a common variant of Verlet integration known as the *leapfrog algorithm*, which can also be implemented in LAMMPS. However, in practice, it is sufficient for many applications to use LAMMPS's standard velocity Verlet algorithm.

2.2 Constraint Dynamics

The basic method described so far should, in principle, allow us to predict the time-evolution of a molecular system. However, the dynamics of real-world systems are often constrained in ways that are not directly or obviously related to Newton's laws. This motivates the implementation of *constraint dynamics*. In particular, we are often interested in simulating systems that have a fixed temperature, which necessitates a *thermostat*. To simulate molecules, which contain multiple atoms in a prescribed geometry, we must also employ a *holonomic constraint* on the atoms within each molecule to maintain this geometry.

2.2.1 Thermostats

If we wish to conduct a simulation in the *canonical ensemble* (in other words, we wish to hold constant the particle number N, the system volume V, and the temperature T), it may be difficult to maintain a constant temperature since symplectic integration only preserves total system energy. This motivates the use of *thermostats* in MD simulations to maintain a desired system temperature. We discuss here two common methods of thermostatting an MD simulation, both of which are simple to implement in LAMMPS:

1. The Berendsen thermostat [44]: This method relies on rescaling velocities to achieve the desired temperature. In the simplest sense, this thermostat can

be implemented by adjusting every atom's velocity $\vec{u}$ to a modified velocity $\vec{u}'$ given by:

$$\vec{u}' = \vec{u}\sqrt{\frac{T_{\text{des}}}{T_{\text{inst}}}} \tag{2.4}$$

where T_{des} is the desired temperature and T_{inst} is the current system temperature. To prevent sharp jumps in temperature, it is common to introduce a relaxation parameter α (less than 1) to "smooth out" the thermostatting process:

$$\vec{u}' = \vec{u}\sqrt{\left(1 + \alpha\left(\frac{T_{\text{des}}}{T_{\text{inst}}} - 1\right)\right)} \tag{2.5}$$

2. The Nosé-Hoover thermostat [45, 46]: This is an "extended-system method" that adds an external heat bath as an additional degree of freedom. This is accomplished by modifying the underlying equations of motion to include a frictional term that guides the system toward the desired temperature:

$$m_i \frac{d^2\vec{r}_i}{dt^2} = \vec{f}_i - \zeta\vec{p}_i \tag{2.6}$$

$$\frac{d\zeta}{dt} = \frac{k_B g}{Q}(T_{\text{inst}} - T_{\text{des}}) \tag{2.7}$$

where Q is the reservoir inertia, g is the number of degrees of freedom in the system, and k_B is Boltzmann's constant ($k_B = 1.38 \cdot 10^{-23}$ J K^{-1}). Note that the damping term serves as a proportional controller that responds to deviations from the desired temperature. The proportional controller produces oscillations of period $2\pi\sqrt{\frac{Q}{2k_B g T_{\text{des}}}}$ around the desired equilibrium temperature.

2.2.2 Holonomic Constraints on Molecular Geometry

If the time-evolution of each atom within a molecule is calculated without an additional geometric constraint, then over a long period of time, the atoms within the original molecule will very likely stray into an unphysical configuration.

To address this problem, we impose holonomic constraints (i.e. relationships between atomic positions). A very common method to impose such constraints involves *Gauss's least-constraint principle* [47]. To make Newton's equations satisfy given constraints while minimally deviating from Newtonian dynamics (in the least-squares sense), we minimize the action S given by:

$$S = \sum_{i=1}^{N} m_i \left(\frac{d^2 \vec{r}_i}{dt^2} - \frac{\vec{f}_i}{m_i} \right)^2 \tag{2.8}$$

subject to the set of c geometric constraints $\{G_c\}$. This minimization leads to modified equations of motion that govern the time-evolution of the system. A popular implementation of geometric constraints based on this principle is the SHAKE algorithm [48], which minimizes S using Lagrange multipliers.

It is worth noting that in this thesis, we only use Gauss's least-constraint principle to constrain molecular geometries; however, this concept can also be applied to thermostats. In particular, if the constraint is taken to be $\partial T / \partial t = 0$, then the resulting equations of motion are guaranteed to conserve temperature. This technique is known as *Evans thermostat* [47].

2.3 MD Algorithm Flow

Here, we provide a more detailed sketch for how the MD technique is implemented. Specific details about the simulations performed for this thesis are discussed in the following chapter. The basic steps are as follows:

1. Initialize the system by specifying all atomic positions and velocities, as well as all relevant interatomic potentials.

2. To advance to the next timestep, loop over each particle $i \in \{1, \ldots, N\}$ and:

   a) Calculate the force on particle i using the interatomic potentials. Note that this step is particularly computationally expensive, as it could impose computational cost up to $\mathcal{O}(N^2)$ (for the pair potentials considered in this thesis).

b) Update the position and velocity of particle i using velocity Verlet. Note that if one wishes to use the Nosé-Hoover thermostat, then the damping must be incorporated in this update step via a modified acceleration. If one is using the Berendsen thermostat, then rescaling can be done after velocities are updated.

3. Save atomic positions and velocities. If the system is sufficiently equilibrated, one may perform thermodynamic sampling using these trajectories.

4. Return to Step 2 and repeat for as many timesteps as desired.

5. After simulation, trajectories can be post-processed for the purposes of statistical analysis or visualization.

2.4 Interatomic Potentials

We now discuss three interatomic potential models for fluids of interest in this thesis: The Lennard-Jones (LJ) potential (a good model for simple molecules interacting primarily through van der Waals effects), and the SPC/E and TIP4P potentials (two models for water).

2.4.1 The Lennard-Jones Potential

To investigate a molecular-scale system quantitatively, we must begin with a model that governs the energetic interactions of molecules in our system. One of the most popular models is the Lennard-Jones (LJ) potential [49]:

$$V(r) = 4\varepsilon\left[\left(\frac{\sigma}{r}\right)^{12} - \left(\frac{\sigma}{r}\right)^{6}\right] \tag{2.9}$$

Here, $V(r)$ denotes the potential energy between a pair of atoms separated by a distance r. The parameters ε and σ serve as characteristic energy and lengthscales (respectively) for the potential; in particular, ε is the magnitude of the minimum

value of the LJ potential and $\sigma\sqrt[6]{2}$ is the interatomic spacing at which this minimum potential is achieved. This potential captures two key features of intermolecular interactions:

1. Strong repulsion ($\mathcal{O}(r^{-12})$) for small separation distances ($r \to 0$), which is due to quantum-mechanical restrictions on heavily overlapping electron clouds.

2. Weak attraction ($\mathcal{O}(r^{-6})$) for large separation distances ($r \to \infty$), which is due to electrostatic interactions between induced dipoles. This attraction is commonly referred to as the van der Waals effect.

In Table 2.1, we list these values for the LJ fluid considered in this thesis, as well as for the carbon atoms within the CNT. The parameters for monoatomic oxygen are taken from models of water (described below) that treat the oxygen atom itself as a LJ atom.

Molecule	σ [Å]	ε [kJ/mol]	Reference(s)
Carbon	3.40	0.3598	[50]
Oxygen (monoatomic)	3.15	0.6364	[51, 52]

Table 2.1: Values for σ and ε for the LJ potentials that are used to model carbon and monoatomic oxygen.

To calculate LJ parameters for interactions between two different types of molecules X and Y, it is very common to use the Lorentz-Berthelot mixing rules [53, 54]:

$$\sigma_{XY} = \frac{1}{2}(\sigma_X + \sigma_Y) \tag{2.10}$$

$$\varepsilon_{XY} = \sqrt{\varepsilon_X \varepsilon_Y} \tag{2.11}$$

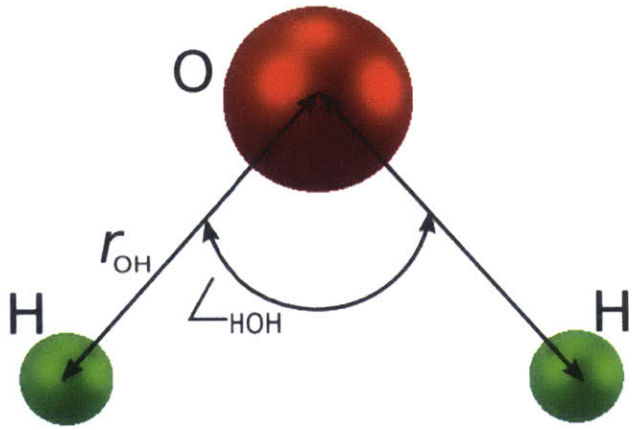

Figure 2-1: Schematic of the SPC/E model for the water molecule, from [2].

r_{OH} [Å]	q_H [e]	q_O [e]	∠HOH [deg]
1.00	0.4238	−0.8476	109.47

Table 2.2: Parameters for the SPC/E water potential.

2.4.2 SPC/E Water Potential

The Extended Simple Point Charge (SPC/E) water potential models the water molecule using 3 distinct sites [52], with a combination of LJ and electrostatic potentials. In particular, the oxygen atom is treated as a LJ atom (with the LJ parameters given above) that also carries electric charge. The hydrogen atoms are treated as point charges. The electrostatic potential between two atoms, carrying charges q_1 and q_2, is calculated using the Coulomb potential:

$$V(r) = \frac{1}{4\pi\varepsilon_0}\frac{q_1 q_2}{r} \tag{2.12}$$

where ε_0 is the electrical permittivity of free space ($\varepsilon_0 = 8.85 \cdot 10^{-12}$ F m^{-1}).

The parameters for this model are listed in Table 2.2. MD simulations that use this model for water must also use the SHAKE algorithm (or another implementation of geometric constraints) to keep the oxygen-hydrogen separation distance and the bond angle constant over time.

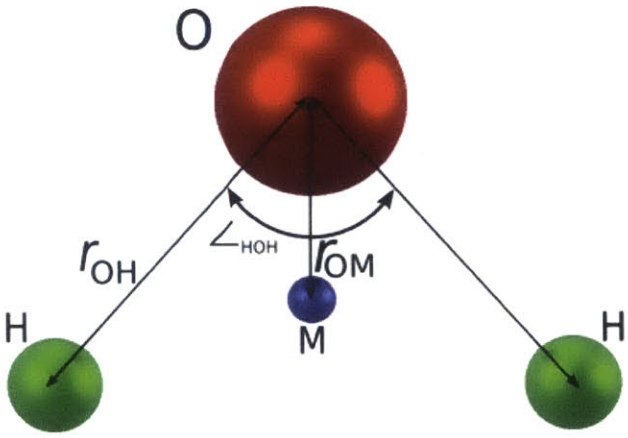

Figure 2-2: Schematic of the TIP4P model for the water molecule, from [3].

r_{OH} [Å]	r_{OM} [Å]	q_H [e]	q_M [e]	∠HOH [deg]
0.96	0.15	0.52	−1.04	104.52

Table 2.3: Parameters for the TIP4P water potential.

2.4.3 TIP4P Water Potential

The TIP4P water potential models the water molecule using 4 distinct sites [51]. In particular, the oxygen atom is treated as an electrostatically neutral LJ atom (with the LJ parameters given above) and the hydrogen atoms are treated as point charges. There is an additional point charge (labeled as M in Figure 2-2) at a "dummy site" between the three "real" atoms. The parameters for this model are listed in Table 2.3. As with the SPC/E model, it is important to use a holonomic constraint to preserve the water molecule geometry over time.

2.5 Sampling of Thermodynamic Quantities from Classical Trajectories

For any system observable A, we can define the expectation value of A as the ensemble average:

$$\langle A \rangle = \int_{\Gamma} A(\{\vec{r}, \vec{p}\}) f(\{\vec{r}, \vec{p}\}) d\Gamma \tag{2.13}$$

where $\{\vec{r}, \vec{p}\}$ is the set of positions and momenta for all particles in the system and f is the probability density in phase-space Γ.

In equilibrium statistical mechanics, the probability density f can be expressed in terms of the system Hamiltonian $\mathcal{H}(\{\vec{r}, \vec{p}\})$ as:

$$f(\{\vec{r}, \vec{p}\}) = \frac{e^{-\beta \mathcal{H}(\{\vec{r}, \vec{p}\})}}{Q} \tag{2.14}$$

where β is the inverse temperature $(k_B T)^{-1}$. Here, Q refers to the partition function, which is defined as:

$$Q = \int_{\Gamma} e^{-\beta \mathcal{H}(\{\vec{r}, \vec{p}\})} d\Gamma \tag{2.15}$$

Discretely speaking, for an ensemble of M identically prepared systems running in parallel (each of which yields a measurement of the observable A), the expectation value of A is given by

$$\langle A \rangle = \frac{1}{M} \sum_{i=1}^{M} A_i \tag{2.16}$$

because an MD simulation, by construction, produces samples of $f(\{\vec{r}, \vec{p}\})$.

This formulation of expectation value is not particularly efficient for an MD simulation, which evolves a *single system* over time. To get a larger sample size without running many MD simulations in parallel, we can make use of the *ergodic hypothesis*; in other words, we assume that successive snapshots of a thermodynamic quantity over time (for a single system) converge *in distribution* to that same quantity measured over a large number of parallel systems. This hypothesis is, of course, only true in steady state. Given the ergodic hypothesis, M represents the number of snapshots over time (as opposed to the number of identically prepared systems running in parallel).

Now we discuss the specific measurement of several key thermodynamic quantities of interest in this thesis. The density ρ in a volume V is calculated according to:

$$\rho = \frac{1}{V} \sum_{i \in V} m_i \tag{2.17}$$

In the absence of a fluid-center-of-mass flow velocity, the temperature T in a volume V is sampled using the Virial Theorem in three dimensions:

$$T = \frac{1}{3Nk_B} \sum_{i \in V} m_i |\vec{u}_i|^2 \tag{2.18}$$

2.6 Reduced Units

Finally, we note that in the field of molecular simulation, it is usually preferred to report quantities in *reduced units*. For a system of N LJ atoms with parameters σ and ε, we define:

1. The reduced particle density $N^* = N\sigma^3$.
2. The reduced temperature $T^* = \frac{k_B T}{\varepsilon}$.
3. The reduced energy $E^* = \frac{E}{\varepsilon}$.
4. The reduced time $t^* = \sqrt{\frac{\varepsilon}{m\sigma^2}} t$.

Chapter 3

Analytical Modeling of Nanoconfined Fluid Structure

"No, no! The adventures first, explanations take such a dreadful time."

– The Gryphon in *Alice's Adventures in Wonderland*

There are several first-principles methods that can, in theory, predict the equilibrium structure of a dense fluid subject to an external potential, such as the potential imposed by the carbon atoms in a CNT. Most notably, this problem can be studied using either liquid-state density functional theory [55] or the Ornstein-Zernike equation in conjunction with an approximate closure relation [56]. In some cases, additional information about equilibrium structure can be obtained through careful geometric considerations [57, 58]. However, with the exception of a few very simple models, neither of these approaches can be pursued analytically; moreover, numerical solutions for the equations that arise from both techniques tend to be very computationally expensive to calculate. Thus, we seek to develop a simple model for nanoconfined fluid structure that requires substantially lower analytical and computational overhead.

In this chapter, we develop theoretical predictions for the structure of a fluid confined within a CNT using a mean-field energetics approach, which does not face any of the difficulties outlined above. We begin by describing the geometry of and notational conventions for CNTs. We also discuss the concept of a fluid radial density function, which will guide our development of a mean-field potential for fluid within a CNT. Through analytical manipulation of the mean-field potential, we proceed to

develop predictions for the characteristic lengthscales associated with fluid confinement. In particular, we propose a model that gives the locations and widths of the fluid rings that form within a CNT, as shown in Figure 1-2. We conclude by describing a method of combining these analytical predictions with results from molecular dynamics simulations, which allows us to infer the density of each fluid ring.

3.1 Theoretical Background

3.1.1 The Structure of a CNT

A single-walled CNT (SWCNT) can be thought of as a sheet of graphene rolled into a cylindrical geometry. The specific configuration of this rolling is given by a pair of integer indices (n, m), also known as the CNT *chiral vector*. These concepts are illustrated in Figure 3-1 (a). In particular, this diagram shows an "unraveled CNT" atop a plane of graphene (one can imagine forming the CNT by cutting along the dotted lines and joining these lines together in a cylinder with circumference equal to the length of $\overline{AA'}$). The chiral vector is formed by:

1. Selecting a carbon atom that falls on a dotted line (Point A).
2. Tracing along one of the graphene basis vectors (denoted as $\vec{a}_1$) until reaching a point of intersection with the other dotted line.
3. Identifying the carbon atom on the opposite dotted line nearest to the point of intersection (Point A').
4. Constructing a vector (denoted as $\vec{c}_h$) pointing from A to A'.

The angle between the chiral vector and the basis vector (used in constructing the chiral vector) is known as the *chiral angle*. Given a CNT chiral vector, we can calculate the CNT's chiral angle θ as well as its radius R using [59]:

$$\theta = \tan^{-1}\left(\frac{m\sqrt{3}}{m+2n}\right) \tag{3.1}$$

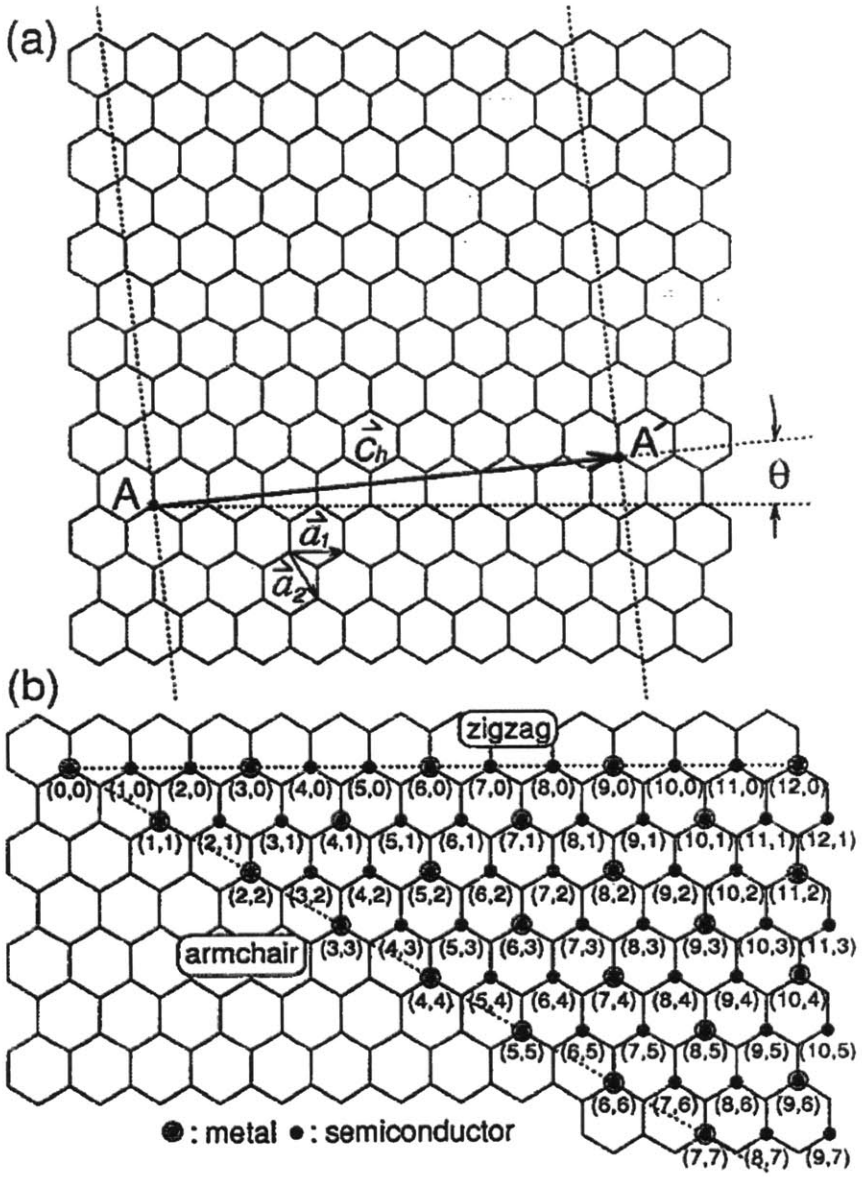

Figure 3-1: Illustration of correspondence between cylindrical CNT geometry and planar graphene geometry, from [4]. Above, we see the relationship between the chiral angle θ and the chiral vector $\vec{c}_h$. Below are a large number of chiral vectors (n, m) shown on the graphene sheet.

$$R = \frac{a\sqrt{3}}{2\pi}\sqrt{n^2 + m^2 + nm} \tag{3.2}$$

where $a \approx 1.421\mathring{A}$ is the distance between carbon atoms in graphene.

The geometries corresponding to several values of θ bear special names. In particular, a CNT with $\theta = 0^o$ is called a *zigzag* CNT; a CNT with $0^o < \theta < 30^o$ is called a *helical* CNT; and a CNT with $\theta = 30^o$ is called an *armchair* CNT. These geometries are illustrated in Figure 3-1 (b). Note that given a fixed θ, the spectrum of possible values for R is discrete since n and m must be integers.

3.1.2 Fluid Radial Density Function (RDF)

The fine details of the fluid structure inside the CNT – which are responsible for the anomalously low average density ρ – can be quantitatively captured by a radial density function (RDF), denoted here by $h(r)$. This quantity is defined such that $A\rho h(r)dr$ is equal to the number of fluid atoms whose molecular centers fall between r and $r + dr$, where r represents the distance from a fixed reference location. Here, A refers to the area of the generalized surface formed by the locus of points at constant r. For example, if the fixed reference location is a point in space, then $A = 4\pi r^2$, the surface of a sphere; if the fixed reference location is the central axis of a CNT of length l, then $A = 2\pi rl$, the surface area of a cylinder.

We note that this definition is similar to, but different from, that of the radial distribution function, commonly denoted as $g(r)$. The radial distribution function is frequently used in molecular simulation to study short-range order in materials; in particular, it quantifies the average distance between molecular centers [56]. Because of its definition, $g(r)$ uses (and averages over) molecular locations as reference locations. In contrast, for our purposes, the primary interest is the fluid structure with respect to a fixed location in space – namely, the CNT wall. In what follows, $h(r)$ uses the CNT central axis as the fixed reference location. This is slightly more

conceptually convenient but clearly an equivalent choice to selecting the CNT wall (located at a fixed distance R from the CNT central axis) as the reference location. According to the definition given above, we expect $h(r)$ to feature peaks and valleys as $r \to R$, reflecting the density variations associated with the ring structure observed close to CNT walls.

3.2 Deriving a Mean-Field Potential Within a CNT

Throughout this work, we will denote interactions between a LJ atom and a carbon atom using the parameters ε and σ; interactions between two LJ fluid atoms will be denoted by ε_f and σ_f. When the fluid of interest is water, these parameters refer to the water molecule's oxygen atom, which is treated as a LJ atom in all of the water models discussed in Chapter 2.

Consider a CNT that is sufficiently long compared to its radius R and whose radius is sufficiently large so that the CNT may be approximated as cylindrical. Under these assumptions, we can adapt the method followed in [60] to derive a mean-field interaction potential $\mathcal{V}(r)$ acting between the CNT wall and a fluid atom at distance r from the CNT axis by integrating the LJ potential around the cylindrical geometry of the CNT:

$$\mathcal{V}(r) = n\pi^2\varepsilon\sigma^2\left[\frac{63}{32}F_{-\frac{9}{2}}(\delta^2)\left(\frac{R(1-\delta^2)}{\sigma}\right)^{-10} - 3F_{-\frac{3}{2}}(\delta^2)\left(\frac{R(1-\delta^2)}{\sigma}\right)^{-4}\right] \quad (3.3)$$

Here, n is the areal density of carbon atoms in the CNT wall, δ is the normalized radius $\delta \equiv r/R$, and $F_\eta(z) \equiv F_{\eta;\eta;1}(z)$ is the Gauss hypergeometric function [61], given by:

$$F_{\alpha,\beta,\gamma}(z) = \sum_{n=0}^{\infty} \frac{(\alpha)_n(\beta)_n}{(\gamma)_n}\frac{z^n}{n!} \quad (3.4)$$

where $(x)_n$ is the rising Pochhammer symbol, defined by $(x)_n = x(x+1)\ldots(x+n-1)$.

The mean-field potential for a variety of CNT radii is shown in Figure 3-2. Note that every potential in this family of curves rises very sharply as $r \to R$, thus leading

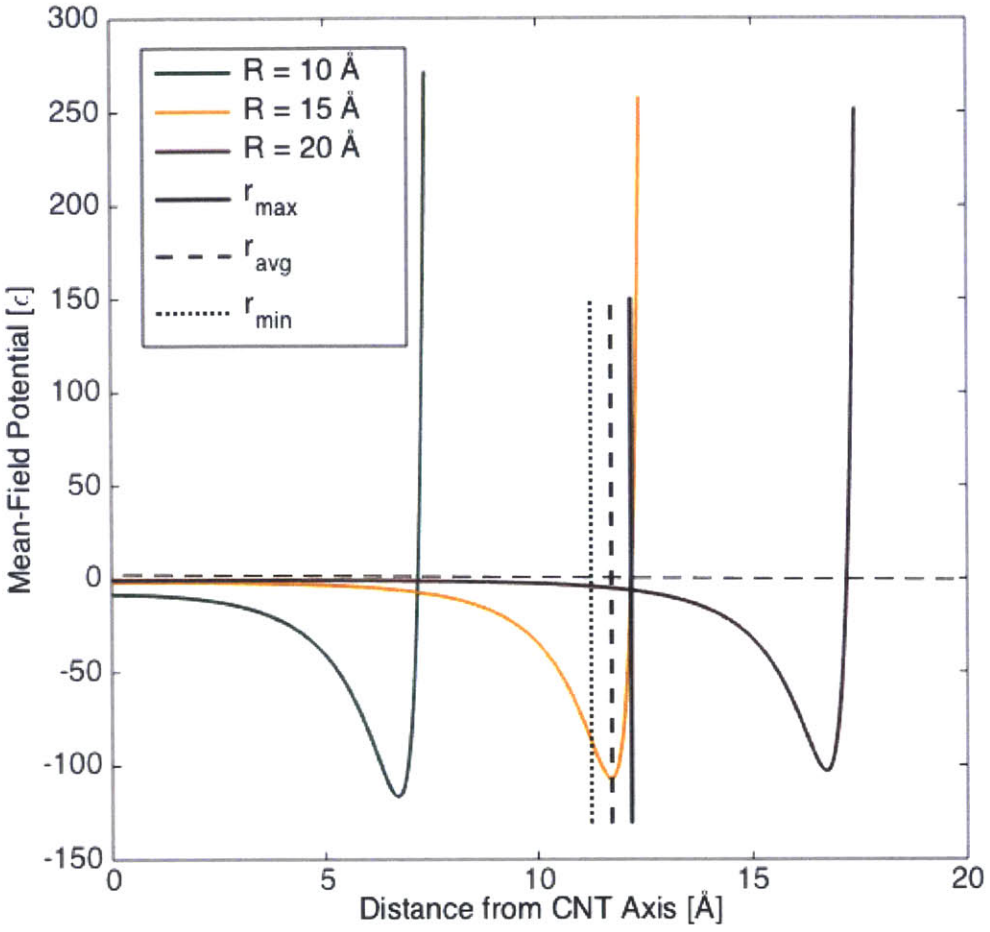

Figure 3-2: Mean-field potentials due to CNTs of three different radii; $r_{\max}$, r_{avg} and $r_{\min}$ are labeled for CNT with $R = 15\mathring{A}$.

to a maximum radius that is energetically accessible to the fluid. This radius will be referred to as $r_{\max}$. Our work below exploits this very steep rise in the mean-field potential to obtain an analytical result for $r_{\max}$. In larger CNTs, where multiple rings form (as is the case in Figure 1-2), $r_{\max}$ will represent the outer radius of the first ring.

3.3 Characteristic Lengthscales for Nanoconfined Fluids

3.3.1 Maximum Accessible Radius

We begin by considering CNTs that are sufficiently large for fluid imbibition to occur (CNT with $R \approx 5\mathring{A}$ are the smallest ones that exhibit single-file imbibition [1]). For these CNTs, we define the *maximum accessible radius* $r_{\max}$ ($r_{\max} < R$) as the location near the CNT wall where the fluid RDF vanishes. In other words, in equilibrium, no fluid molecules are found within the CNT at a radius greater than $r_{\max}$.

We calculate the maximum accessible radius $r_{\max}(R, \sigma, \varepsilon, T)$ by finding the location at which most of the fluid molecules have insufficient kinetic energy to overcome the potential barrier $\mathcal{V}(r)$. The steep rise of $\mathcal{V}(r)$ close to $r = R$ (where $r_{\max}$ is expected to lie) allows us to approximate this location by $\mathcal{V}(r_{\max}) = 0$ with little error for typical LJ parameters ε and σ and temperature T. A direct consequence is that our solution for $r_{\max}$ is independent of the temperature.

Setting $\mathcal{V}(r_{\max}) = 0$, we can rearrange Eqn. (3.3) into:

$$\frac{21}{32}\sigma^6 = R^6\left(1 - \delta_{\max}^2\right)^6 \frac{F_{-\frac{3}{2}}\left(\delta_{\max}^2\right)}{F_{-\frac{9}{2}}\left(\delta_{\max}^2\right)} \tag{3.5}$$

where $\delta_{\max} = r_{\max}/R$. This equation shows that the parameter ε can be scaled out of the problem and thus $\delta_{\max} = \delta_{\max}(R, \sigma)$. To solve, we make the ansatz:

$$\delta_{\max} = 1 - k_{\max}\sigma/R \tag{3.6}$$

where $k_{\max}\sigma$ is the stand-off distance from the CNT wall and $k_{\max} = k_{\max}(R, \sigma)$. This choice is motivated by the expectation that the standoff distance will be of order σ. Inserting the above expression for $\delta_{\max}$ in Eqn. (3.5) we obtain to leading order:

$$k_{\max}(R, \sigma) = (2/5)^{1/6} \tag{3.7}$$

Here, we have used a theorem due to Gauss [61] to expand the hypergeometric

function near $\delta_{\max} = 1$ in the form:

$$F_{\alpha;\beta;\gamma}(\delta^2_{\max}) = \frac{\Gamma(\gamma)\Gamma(\gamma-\alpha-\beta)}{\Gamma(\gamma-\alpha)\Gamma(\gamma-\beta)}\left(1+\mathcal{O}\left(\frac{\sigma}{R}\right)\right) \tag{3.8}$$

Having solved for $k_{\max}$, we can write:

$$r_{\max}(R,\sigma) = R - (2/5)^{1/6}\sigma \tag{3.9}$$

The leading-order solution obtained here is equivalent to neglecting the effect of CNT curvature (i.e. $\sigma/R \ll 1$), which explains why the stand-off distance $r_{\max}$ is not a function of R. Although it is possible to include higher-order terms that couple to the CNT curvature, the excellent agreement of Eqn. (3.9) with numerical solution of Eqn. (3.5) for $R > 5\mathring{A}$ (presented in Chapter 5) suggests that higher-order terms are unnecessary.

3.3.2 First Ring Thickness and Inner Radius

In this section we consider CNTs that are sufficiently large ($R > 6\mathring{A}$) that at least one fluid ring can form within the CNT cross-section. In this case, $r_{\max}$ will correspond to the outer radius of this ring. To describe the thickness of the ring, we also need the ring inner radius. This quantity can be calculated by again exploiting the shape of $\mathcal{V}(r)$ as $r \to \infty$. Specifically, we assume that the first ring is centered in a symmetric fashion around the minimum of $\mathcal{V}(r)$, denoted by r_{avg}. We estimate the half-width of this ring as $r_{\max} - r_{\text{avg}}$, and so the location of the inner radius can be calculated as:

$$r_{\min} = 2r_{\text{avg}} - r_{\max} \tag{3.10}$$

The value of r_{avg} is obtained by setting the derivative of Eqn. (3.3) to zero and is

given by:

$$\frac{\delta_{\text{avg}}}{R^{11}}\left[\frac{81F_{-\frac{7}{2}}(\delta_{\text{avg}}^2)}{2(1-\delta_{\text{avg}}^2)^{10}}+\frac{20F_{-\frac{9}{2}}(\delta_{\text{avg}}^2)}{(1-\delta_{\text{avg}}^2)^{11}}\right]- \frac{32\delta_{\text{avg}}}{21\sigma^6R^5}\left[\frac{9F_{-\frac{1}{2}}(\delta_{\text{avg}}^2)}{2(1-\delta_{\text{avg}}^2)^{4}}+\frac{8F_{-\frac{3}{2}}(\delta_{\text{avg}}^2)}{(1-\delta_{\text{avg}}^2)^{5}}\right]=0 \tag{3.11}$$

where $\delta_{\text{avg}} = r_{\text{avg}}/R$.

Following the same argument as in the previous section, we write δ_{avg} in the form:

$$\delta_{\text{avg}}(R,\sigma) = 1 - k_{\text{avg}}\sigma/R \tag{3.12}$$

where $k_{\text{avg}} = k_{\text{avg}}(R,\sigma)$. We can solve Eqn. (3.11) by substituting Eqn. (3.12) and neglecting terms smaller than $\mathcal{O}(R/\sigma)$ to obtain:

$$\frac{21}{32}\sigma^6 = \frac{\frac{256}{3\pi}R\Big(2k_{\text{avg}}\sigma\Big)^{-1}}{\frac{524288}{63\pi}R\Big(2k_{\text{avg}}\sigma\Big)^{-7}} \tag{3.13}$$

which simplifies to $k_{\text{avg}} = 1$. Note that omitting terms that are smaller than $\mathcal{O}(R/\sigma)$ relies again on the assumption that $\sigma/R \ll 1$.

This means that the midpoint of the outermost ring is at a distance σ from the CNT wall. Therefore, by symmetry, we can estimate the inner radius of the outermost ring as:

$$r_{\text{min}} = R - k_{\text{min}}\sigma \tag{3.14}$$

where $k_{\text{min}} = 2 - (2/5)^{1/6}$.

In the following section we show how this methodology can be extended to the description of subsequent rings that appear as the CNT radius increases.

3.3.3 Subsequent Rings

Now we consider CNTs for which there are at least two distinct rings (empirically, $R > 9\mathring{A}$). We capture the geometry of additional rings within the outermost ring by

recognizing that the outermost ring itself can be treated as another CNT. The key insight here is that the perfect solid ordering of atoms within the CNT wall leads to near-solid ordering of fluid near the CNT wall (Figure 3-3). In fact, this general approach of recognizing that a cylindrical solid structure induces concentric near-solid ordering in adjacent fluid has been pursued with success by Koga and Wilson in numerous molecular dynamics studies [27, 62, 63].

We denote the outermost ring's outer radius by $r_{(1),\max}$ and its inner radius by $r_{(1),\min}$. Then a bound for the second ring's outer radius is:

$$r_{(2),\max} = r_{(1),\max} - k_{\max}\sigma_f \tag{3.15}$$

Similarly, a bound for the second ring's inner radius is:

$$r_{(2),\min} = r_{(1),\min} - k_{\min}\sigma_f \tag{3.16}$$

This bounding process can be repeated indefinitely to fix outer and inner radii for the n-th ring $r_{(n)}$, but in practice this method loses meaning after the outer radius of the $(j+1)$-st ring is greater than the inner radius of the j-th ring, at which point the rings are "blurred" into a more uniform background bulk structure. The intuition behind this "blurring" phenomenon is that fluid within the CNT that is sufficiently far away from the CNT wall will not be "aware" of the presence of the wall. Thus, fluid near the center of the CNT (which we will term the "bulk core" of the fluid) will generally resemble bulk fluid in terms of thermodynamic properties. For the purposes of later calculations, we will only consider the formation of two rings before relaxation to the bulk structure.

3.4 Extracting Ring Densities through Molecular Dynamics Simulation

Thus far, we have developed a model for where rings will form within a CNT, but we do not know *how dense* the fluid within these rings will be. Given this information, we will be able to calculate the overall density of the confined fluid, which in turn

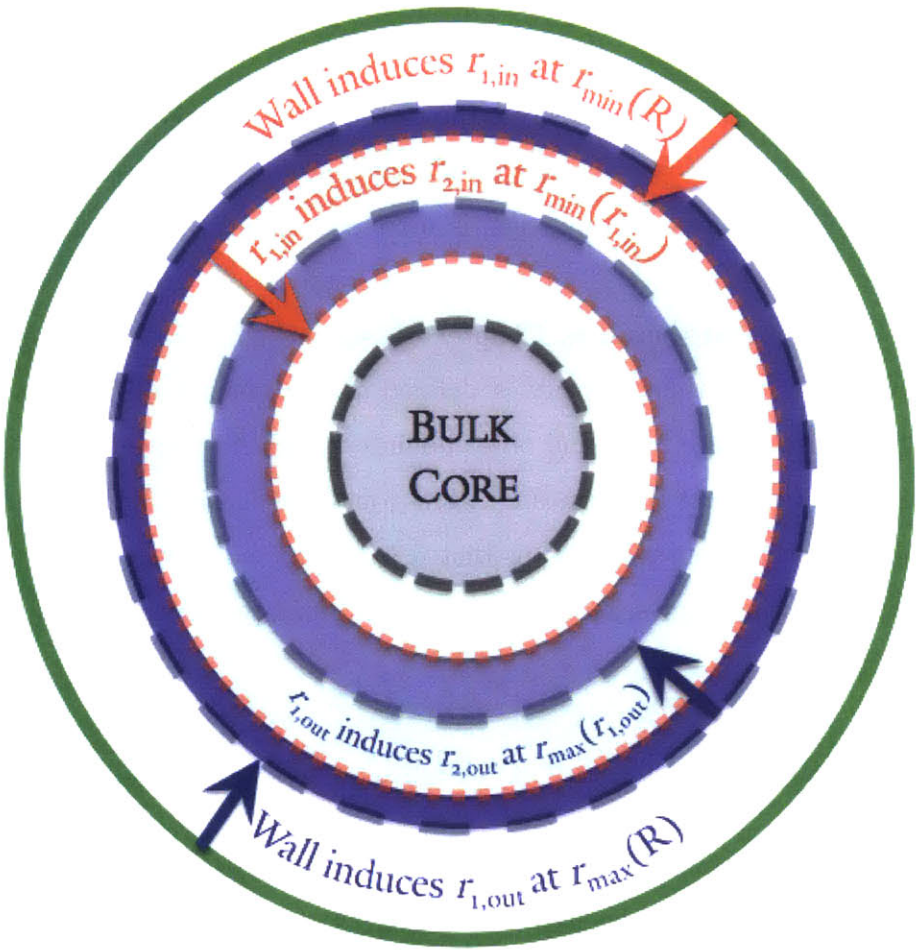

Figure 3-3: Schematic representation of model for ring formation. Fluid rings are denoted by blue and CNT wall is denoted by green.

enables us to quantify the magnitude of the anomalous density. Though one may be tempted to guess that fluid within the rings will simply be at the bulk density, it is important to remember that each ring of fluid has equilibrated in the presence of a non-negligible external potential given by Eqn. (3.3). As such, the density of each ring is *higher* than the bulk density, since it is energetically preferable for the fluid to arrange itself such that fluid atoms are positioned within the mean-field potential valley.

The analytical methods discussed in the introduction of this chapter could, in principle, be used to calculate the magnitude of these ring densities. However, we propose here an alternative method that is more conceptually straightforward and less computationally expensive. By conducting a small set of equilibrium molecular dynamics simulations (discussed in Chapter 4), we can empirically determine the densities of each ring. Here, density is defined as the number of fluid molecular centers falling between the inner and outer bounds of each ring, given above.

The density of the first (outermost) ring $\rho_{(1)}$ and the density of the second ring $\rho_{(2)}$ can be used in tandem with the predicted locations and widths of the rings to construct the following expression for the overall (normalized) density as a function of CNT radius:

$$\rho(R) = \frac{1}{R^2}\left((r^2_{(1),\max} - r^2_{(1),\min})\rho_{(1)} + (r^2_{(2),\max} - r^2_{(2),\min})\rho_{(2)} + r^2_{(3),\max}\right) \qquad (3.17)$$

Figure 3-4 provides a schematic illustration of this process for calculating the overall density. Note that this density is normalized against the bulk density ρ_{bulk}, since the density of the bulk core (i.e. the fluid at a distance $0 < r < r_{(3),\max}$ from the CNT axis) is set to unity here but the "actual" density of the bulk core is ρ_{bulk}.

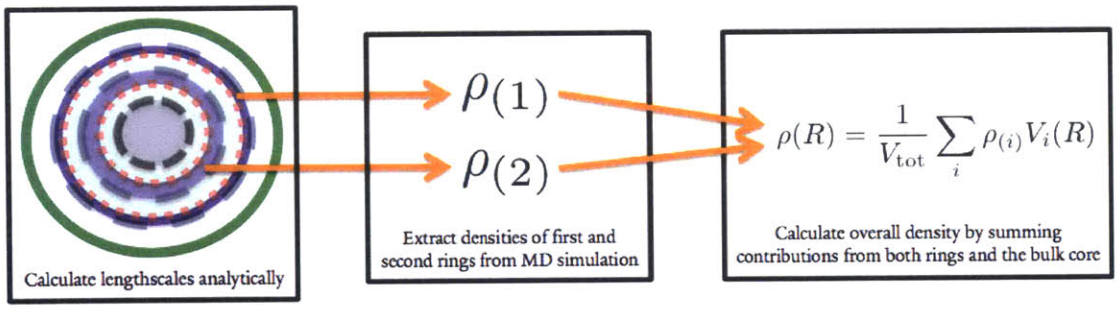

Figure 3-4: Schematic of the method for calculating the overall density in a CNT of radius R.

Chapter 4

MD Simulation Details

"Because the truth of the story lies in the details... I have no choice but to tell the story exactly as it happened.

– Paul Auster in *Brooklyn Follies*

In this chapter, we discuss how MD simulations were performed using the Large-scale Atomic/Molecular Massively Parallel Simulation (LAMMPS) code [43]. In particular, we detail our system initialization (including the definition of atoms and the construction of an initial set of atomic positions and velocities), relevant simulation settings, and the post-processing of simulation output.

4.1 Initialization of the CNT-Reservoir Geometry

To study the equilibrium density of a fluid confined within a CNT, we used the simulation geometry of a single CNT immersed within an isothermal *fluid bath* (reservoir) subject to periodic boundary conditions. In particular, by fluid bath, we mean a fixed (and large) number of fluid molecules within a fixed volume. This geometry can be seen in Figure 4-1. We performed simulations using two different kinds of fluids: Lennard-Jones fluid and TIP4P water (simulations were also performed using the SPC/E model to check for agreement with the TIP4P model).

The simulated CNTs were of radii ranging from $9\mathring{A}$ to $35\mathring{A}$. All CNTs were of armchair chirality; it has been shown that chirality has no observable impact on equilibrium fluid density within a CNT [1, 6]. The CNT was kept rigid throughout each

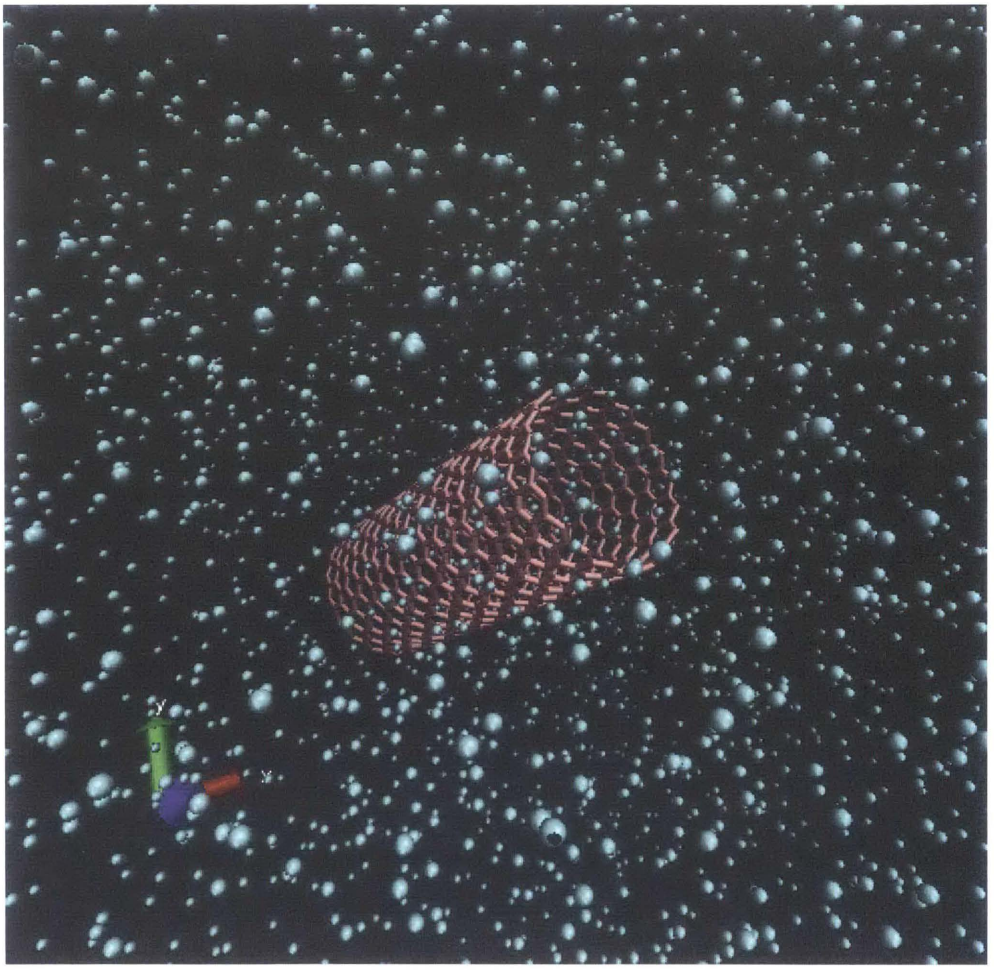

Figure 4-1: Snapshot of CNT in LJ fluid bath, visualized in VMD.

simulation by setting the temperature of all carbon atoms to zero; it has been shown that thermally oscillating CNT walls have only a small impact on equilibrium fluid structure and density [64]. To mitigate end effects on the calculation of equilibrium fluid density within the CNT, the length of each CNT was between 2.8 and 3.1 times its diameter.

The fluid bath was initialized as a simple cubic lattice (except for near the CNT, where a small amount of space was left open to prevent overlapping atoms). LJ fluid atoms and water molecules were initialized using the geometric and energetic parameters presented in Chapter 2. Initial fluid velocities were drawn from the Maxwell-Boltzmann probability density function corresponding to T =300 K:

$$f(v_x, v_y, v_z) = \left(\frac{m}{2\pi k_B T}\right)^{3/2} e^{-\frac{m(v_x^2+v_y^2+v_z^2)}{2k_B T}} \tag{4.1}$$

For LJ fluids, we performed simulations using three different fluid bath densities: $\rho_{\text{bulk}} \in \{0.8\sigma_f^{-3}, 1.0\sigma_f^{-3}, 1.1\sigma_f^{-3}\}$; for water, the fluid bath density was chosen to match 1000 kg m^{-3}, the bulk density of liquid water.

To ensure that the finite bath size did not affect simulation results, the size of the reservoir was at least twice the size of the CNT in each dimension. The reservoir volume was $100\mathring{A} \times 100\mathring{A} \times 120\mathring{A}$ for CNTs with $R < 20\mathring{A}$ and $100\mathring{A} \times 100\mathring{A} \times 200\mathring{A}$ for CNTs with $R > 20\mathring{A}$. These volumes were chosen so that the density change in the reservoir due to CNT imbibition was negligible. To facilitate convergence to equilibrium density, CNTs were pre-filled to a relative density of 0.2 (i.e. 20% of the reservoir density).

For the LJ fluid, we also tested the effect of varying ε by conducting simulations over a decade of ε – in particular, $\varepsilon \in \{0.05, 0.10, 0.25, 0.50\}$ kJ mol^{-1}.

4.2 Simulation Settings

4.2.1 Thermostat

Simulations were conducted at 300 K in LAMMPS in the NVT (canonical) ensemble coupled to a Berendsen thermostat. Additional simulations were performed at 100K and 400K to ensure that the excluded-region lengthscales have no dependence on temperature. Simulations using the Nosé-Hoover thermostat were also performed to check that the choice of thermostat did not affect equilibrium fluid structure or density within the CNT.

4.2.2 Cutoff Distance

To reduce computational cost, all simulations made use of a *cutoff distance*. In other words, when determining the net force on an atom, only neighboring atoms within a specified radius were included in the calculation. A cutoff distance of 3σ was used throughout all simulations. Additional simulations were performed with cutoff distances of 4σ and 5σ to ensure that results did not depend on the cutoff.

4.2.3 Relevant Timescales

The simulation time step was 2.0 fs. Each system was initially thermostatted and allowed to equilibrate for 2.0 ns, after which the thermostat was turned off. Atomistic kinematics were then recorded every 2.0 fs for a total of 5.0 ns. A small number of simulations were performed with kinematics recorded up to 10.0 ns, which confirmed that 5.0 ns was sufficient for the fluid within the CNT to converge to an equilibrium structure and density.

4.2.4 Output Format

The output file from each simulation contained the following information at each timestep:

1. The x-, y-, and z-coordinates of each atom.

2. The x-, y-, and z-components of velocity for each atom.

3. The temperature, as calculated over all fluid molecules in the system.

4. The kinetic and potential energies of the system.

4.3 Post-Processing of Simulation Output

We performed the following analysis on each simulation output:

1. We identified all fluid molecules within the CNT (imbibed fluid) by comparing fluid atomic positions to the known location of the CNT.

2. By calculating the radial distance of each imbibed fluid molecule from the CNT axis, we calculated (at each timestep) the RDF within the CNT.

3. We calculated the *maximum accessible radius* as the largest distance away from the CNT axis (but within the radius of the CNT) at which the RDF had a non-zero value. In the case of water, this calculation was done separately for oxygen atoms and hydrogen atoms.

4. We applied the model presented in Chapter 3 to predict locations of the fluid rings and the bulk core, given the CNT radius. Each imbibed fluid molecule was then assigned to the ring within which it was located or the bulk core. The small number of fluid molecules not within a ring or the bulk core (approximately 7% of all imbibed fluid molecules) were assigned to the *nearest* ring (or the bulk core, if the molecule was closer to the bulk core than to the second ring).

5. We then computed the density of each ring and the bulk core, as well as the overall density of the imbibed fluid. Note that these densities were all normalized against the reservoir density (i.e. a reported density of ρ corresponds to an actual density $\rho\rho_{\text{bulk}}$).

6. For visualization, we imported simulation output into the software Visual Molecular Dynamics (VMD) [65].

Chapter 5

Results

"Are we there yet? Are we there yet?... Are we there yet?"

– Bart and Lisa in *The Simpsons*

In this chapter, we compare the results of our MD simulations with the models presented in Chapter 3. In particular, we demonstrate that there is very close agreement between the theoretically predicted lengthscales and MD simulation results for both LJ fluids and water. We also show that (in the case of the LJ fluid) the ring-formation model can be coupled to ring densities obtained through MD simulation, yielding accurate predictions of anomalous density as a function of CNT radius. We also present evidence that the concept of excluded volume can play an important role in modeling simple flow phenomena.

5.1 Equilibrium Lennard-Jones Fluid

5.1.1 Qualitative Comparison of Theory and MD Simulation

In Figure 5-1, we show a snapshot of the equilibrium configuration of LJ atoms within a CNT (with $R = 10.18\mathring{A}$), with theoretical predictions for the ring locations overlaid. We observe good qualitative agreement between the analytically calculated lengthscales and the results from MD simulation. In the following sections, we present further quantitative evidence of this close agreement between the model and the MD simulations.

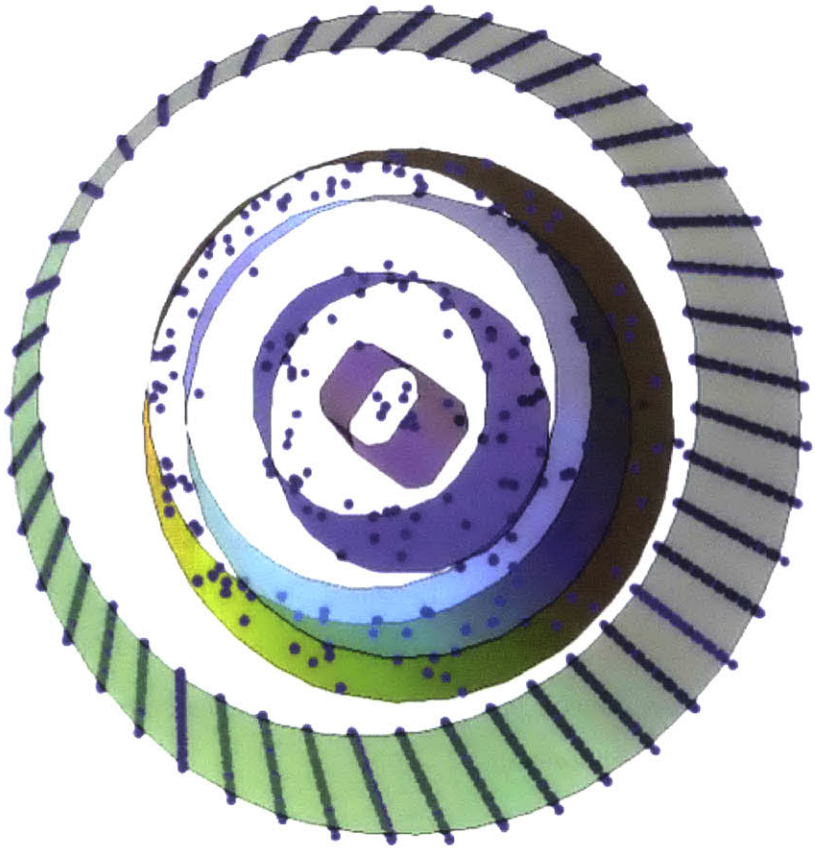

Figure 5-1: Theoretical predictions for ring locations in a CNT (R = 10.18 Å) and equilibrium positions of LJ fluid atoms from MD simulation. For clarity, the outer and inner radii are shown for the outermost ring; only the outer radius is shown for the second ring and the bulk core.

5.1.2 Maximum Accessible Radius

To validate the analytical result in Eqn. (3.9), we calculated maximum accessible radii according to the procedure described in Chapter 4. We also calculated numerical solutions of the equation expressing the energetic condition that defines the maximum accessible radius (Eqn. (3.5)). The results are shown in Figure 5-2. This figure shows that Eqn. (3.9) is in excellent agreement with but also explains our MD results as well as MD results by other groups [8, 29] for $R > 5\mathring{A}$.

5.1.3 Fluid Radial Density Function

Figure 5-3 shows a comparison between the analytically predicted fluid-structure lengthscales and our MD simulation results for a temperature of 300K and $\rho_{\text{bulk}} = 1\sigma_f^{-3}$. We note that the two largest peaks of the RDF, corresponding to the two fluid rings near the wall, are bounded very accurately by the analytical predictions (shown as dashed lines). For radii less than the location of the second RDF peak, we observe that there are still oscillations in the RDF; however, we can see that identifying this region as the bulk core (having average relative density of unity) is a good approximation. The good agreement extends to the whole range of simulations performed in this work ($0.8\sigma_f^{-3} \leq \rho_{\text{bulk}} \leq 1.1\sigma_f^{-3}$ and $100\text{K} \leq T \leq 400\text{K}$).

In agreement with our model prediction, our MD simulations (in the temperature range $100\text{K} \leq T \leq 400\text{K}$) as well as simulations from other groups [35, 36, 64] show negligible dependence of the inner and outer radii of each ring on temperature. We also note that Eqn. (3.9) is valid for a wide range of bulk fluid densities; specifically, we found agreement for the full range of MD simulations conducted (spanning the range $0.8\sigma_f^{-3} \leq \rho_{\text{bulk}} \leq 1.1\sigma_f^{-3}$).

5.1.4 Overall Fluid Density in "Large" CNTs

As discussed in Chapter 3.3.3, we can combine the analytical expressions for ring locations and widths with information from MD simulations about the fluid density inside the first two rings to obtain predictions for the overall nanoconfined fluid density.

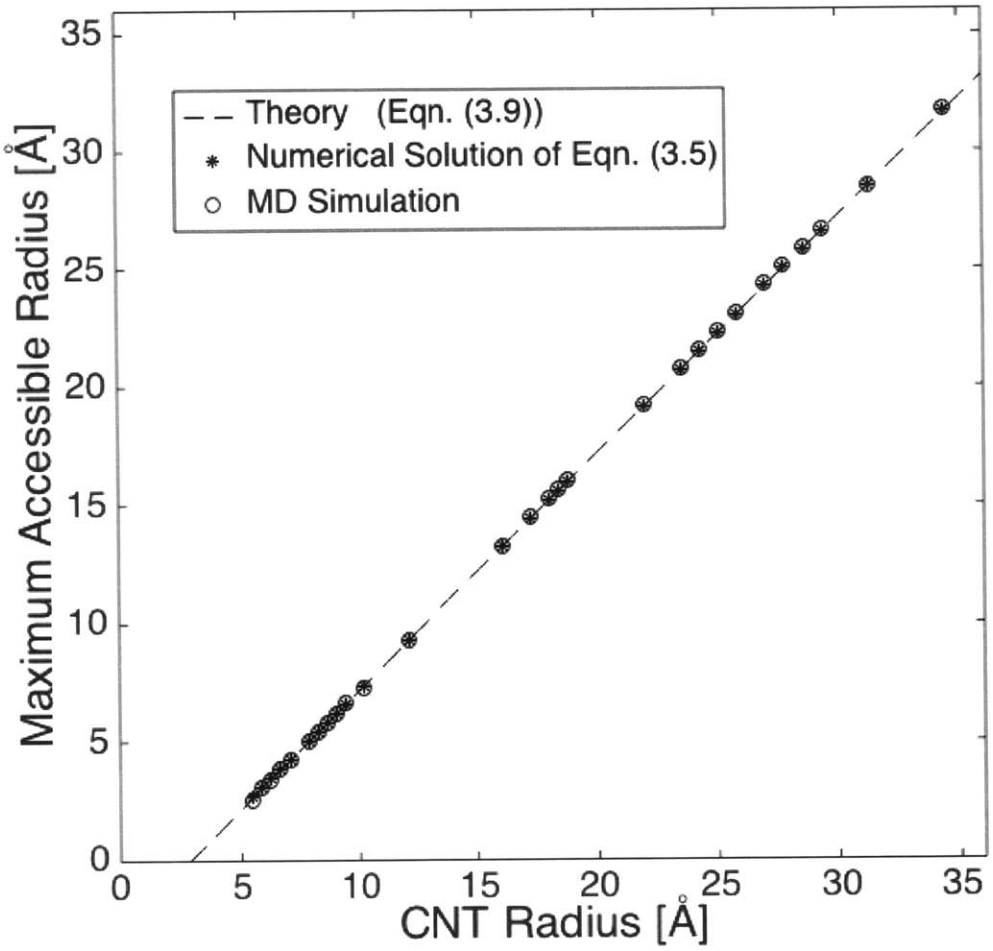

Figure 5-2: Comparison between theoretical prediction for maximum accessible radius given in Eqn. (3.9), numerical solution of Eqn. (3.5), and maximum accessible radius from MD simulations.

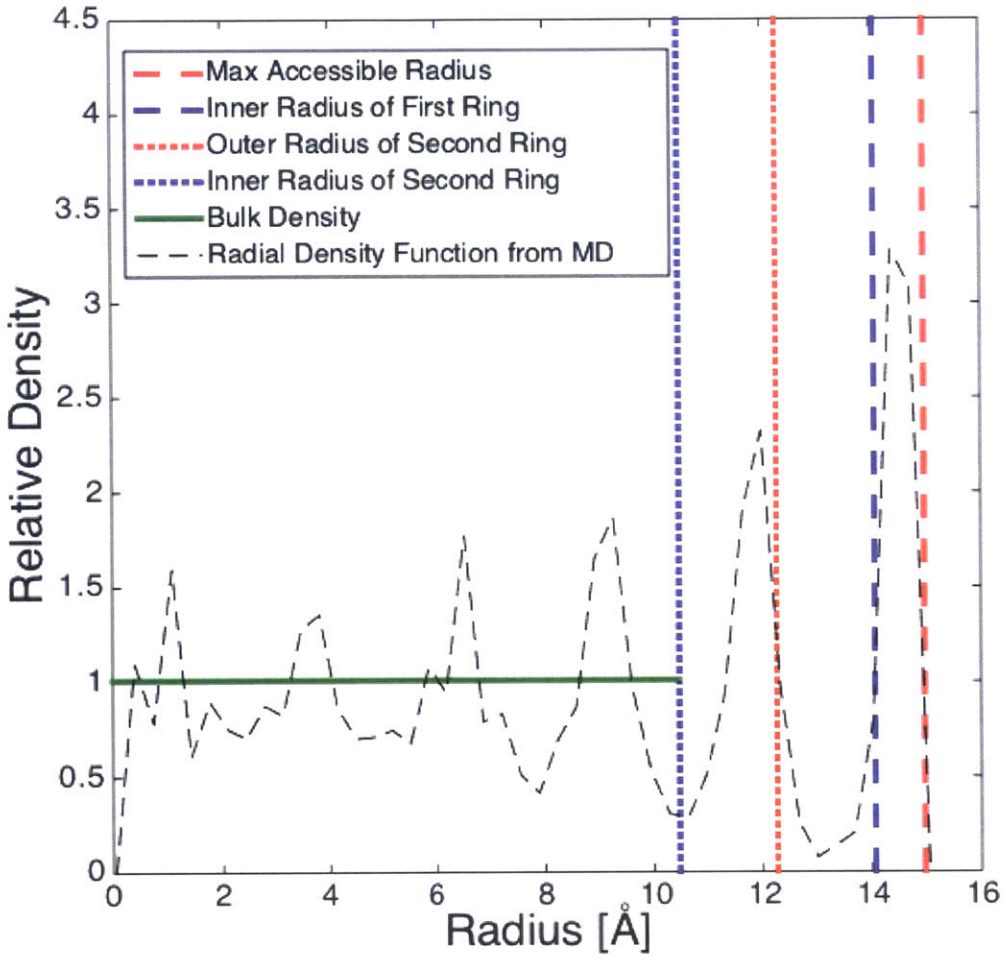

Figure 5-3: Theoretical predictions for ring locations in a CNT (R = 17.61 Å) and radial density profile for LJ fluid from MD simulation.

We calculated the densities of each fluid ring following the procedure outlined in Chapter 4.3. The mean ring densities are reported in Table 5.1. We note that the relatively high densities reported in this table, especially for the outermost ring, are a result of using the volume which encloses all atomic centers to define density. If, for example, one extends this volume by 0.5σ in each direction to account for the true volume occupied by the atoms, the ring densities would be much closer to unity.

Ring	Normalized Density
1st	$\rho_{(1)} = 3.15 \pm 0.04$
2nd	$\rho_{(2)} = 1.40 \pm 0.07$
Bulk core	1.01 ± 0.02

Table 5.1: Densities of each ring, calculated from MD simulation at $T = 300K$, normalized by the bulk density.

Using these ring densities, we can construct a closed-form expression for the equilibrium density of this LJ fluid inside a CNT as a function of the CNT radius using Eqn. (3.17):

$$\rho(R) = \frac{1}{R^2}\Big((r^2_{(1),\max} - r^2_{(1),\min})3.15 + (r^2_{(2),\max} - r^2_{(2),\min})1.40 + r^2_{(3),\max}\Big) \qquad (5.1)$$

It can be readily verified that this expression asymptotically approaches unity (from below) for large R, as expected. Here, it is important to emphasize that this density is normalized by the bulk density ρ_{bulk} of the fluid with which the fluid in the CNT is in equilibrium; in other words, for a CNT placed in a bath of fluid at density ρ_{bulk}, the density of the fluid in a CNT of radius R is $\rho(R)\rho_{\text{bulk}}$.

Figure 5-4 shows that Eqn. (5.1) is in excellent agreement with densities measured in MD simulations at a bulk density of $1.0\sigma_f^{-3}$ and $T = 300$K. For $R > 15\mathring{A}$, the discrepancy is within 3% for all simulated CNTs in the range $0.8\sigma_f^{-3} \leq \rho_{\text{bulk}} \leq 1.1\sigma_f^{-3}$.

It is important to note at this point that the fluid density inside the rings is, in general, dependent on temperature. Therefore, the simulation process must be repeated at each system temperature of interest or the fluid ring densities must be calculated through other means that take temperature into account [57, 58].

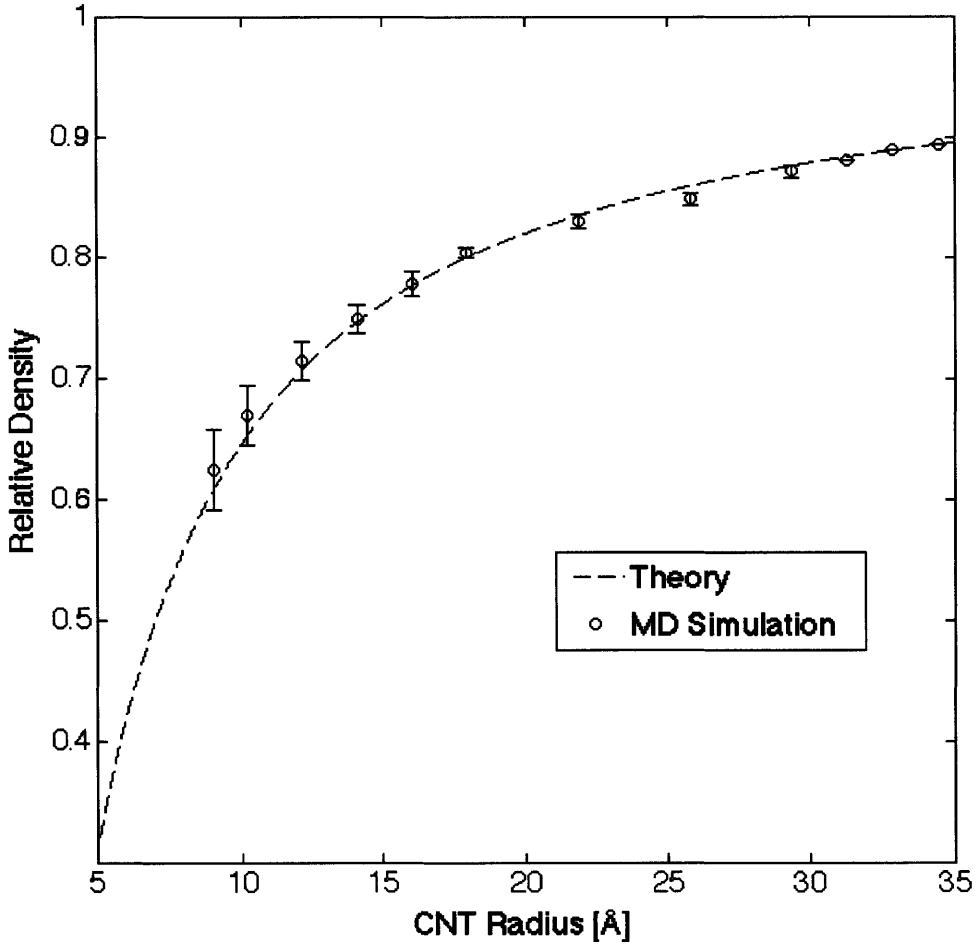

Figure 5-4: Theoretical prediction for $\rho(R)$ with densities measured from MD simulations overlaid.

5.1.5 Effect of Varying ε

We found that variations over a decade of ε (0.05 kJ mol^{-1} $< \varepsilon <$ 0.50 kJ mol^{-1}) resulted in changes in the mean density of each ring that are less than 6% (as compared to results for the baseline value of $\varepsilon = 0.48$ kJ mol^{-1}). In other words, provided the carbon-fluid interaction is within this hydrophobic range, $\rho_{(1)}$ and $\rho_{(2)}$ are approximately independent of ε. We also note that the excluded-region lengthscales exhibit negligible sensitivity to variations in ε, which confirms our intuition that ε scales out of the problem when calculating equilibrium stand-off distances.

5.2 Equilibrium TIP4P Water

5.2.1 Maximum Accessible Radius for Oxygen

We note that in the most common water models for MD simulations (e.g. SPC/E [52], TIP3P [66], TIP4P [51], TIP5P [67], as well as a popular six-site model [68]), the interaction between the oxygen atom and other atoms is described by a LJ potential. Since these models assume that LJ interactions between hydrogen and carbon are negligible compared to LJ interactions between oxygen and carbon, we can use Eqn. (3.9) to predict the point at which the oxygen RDF for water confined within a CNT vanishes.

These predictions agree closely with results from six sets of MD simulations as shown in Fig. 5-5. The analytical prediction given by Eqn. (3.9) is a definite improvement over current approaches found in the literature, which rely on empirical measurements from MD simulations [10, 29]. It is noteworthy that the presence of electrostatic interactions has a remarkably small effect on the prediction of the zero of the oxygen RDF; this is in agreement with the physical basis of our model, which attributes ring formation to the interplay between short-range attractive and repulsive molecular interactions.

We also found that these results did not depend on the water model used – in particular, the maximum accessible radius results were identical for simulations using

the SPC/E model. Moreover, the maximum accessible radius results did not change within the simulated temperature range $100\text{K} \leq T \leq 400\text{K}$.

5.2.2 Maximum Accessible Radius for Hydrogen

This approach can also be used to calculate the maximum accessible radius of hydrogen atoms in water. Since there is no significant interaction between carbon and hydrogen in these water models, the maximum accessible radius of hydrogen is identical to that of oxygen, extended by $0.96\mathring{A}$ (the length of the O-H bond in the TIP4P model). Fig. 5-6 shows that this purely geometric argument captures simulation results accurately. On the other hand, this geometric argument contains no information about the angular distribution of water molecules [29]. As a result, additional ingredients are required before the equilibrium density of water in CNTs can be described analytically with high precision. This will be the subject of future work.

5.3 Application to a Simple Flow Problem

Since non-equilibrium MD simulations have shown that fluid flow does not appreciably modify oxygen and hydrogen RDFs from their equilibrium shapes [8], we can use the equilibrium results obtained above to gain insight into simple non-equilibrium problems. Specifically, these results can be useful in situations where knowledge of the density distribution is useful (e.g. for constructing models of other thermodynamic properties [21, 69, 70, 71]), as well as in cases where fluid flow rates are related to "geometric" effects within the fluid.

5.3.1 The Nanoscale Convergent Nozzle

As an example of such a geometric effect of fluid structure on flow, we consider a nanofluidic system studied by Hanasaki and Nakatani described in Ref. [10] and illustrated in Figure 5-7. This system uses a CNT junction to emulate a nanoscale convergent nozzle, with potential applications in molecular-sensing technology [72]

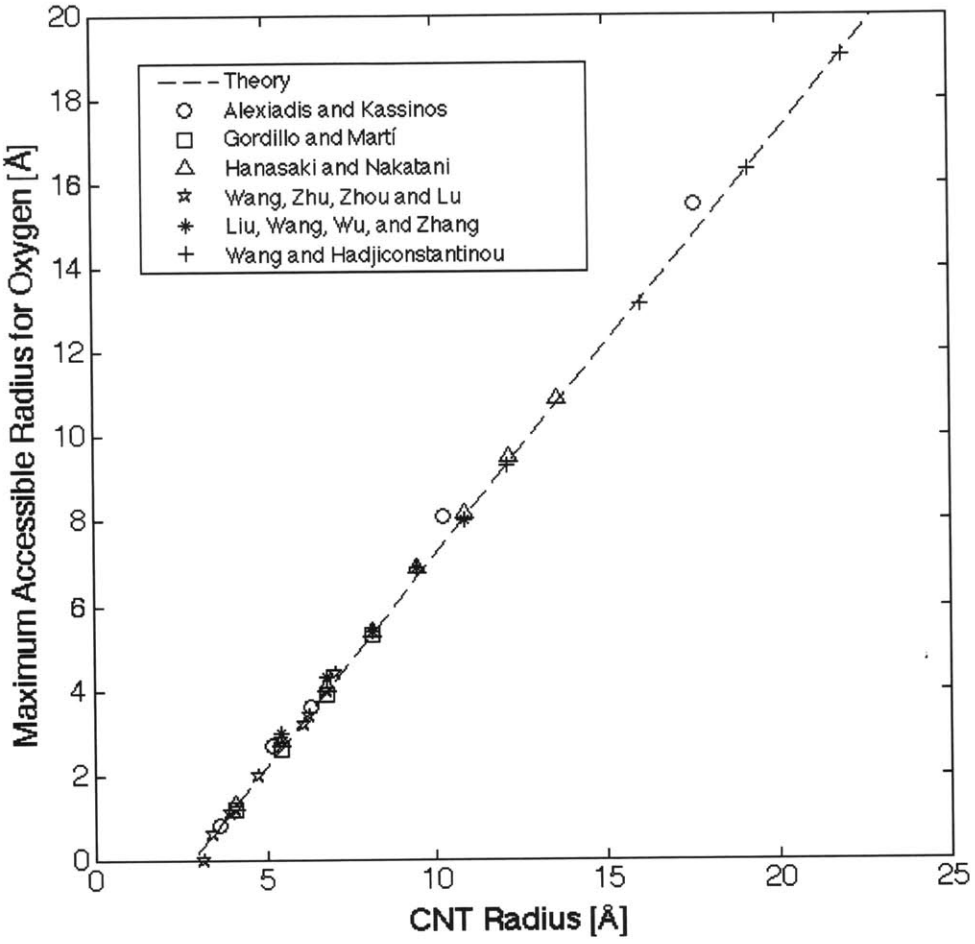

Figure 5-5: Theoretical prediction for maximum accessible radius of the oxygen atom in a water molecule and maximum accessible radius from MD simulations by Refs. [1], [5], [6], [7], and [8], and the author.

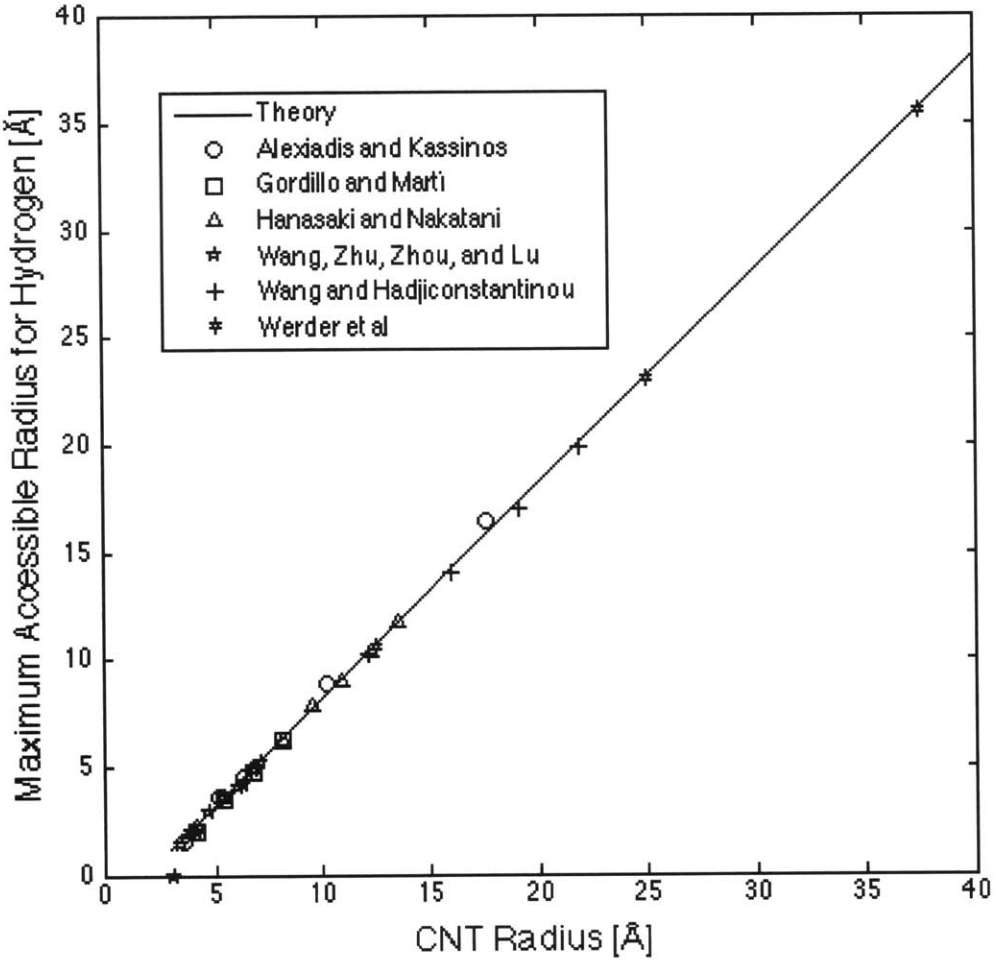

Figure 5-6: Theoretical prediction for maximum accessible radius of the hydrogen atom in a water molecule and maximum accessible radius from MD simulations by Refs. [1], [5], [8], [6], [9], and the author.

and nanoscale hydraulic actuators [73].

These nozzles were constructed by gradually tapering one armchair CNT into another armchair CNT with smaller radius. Water molecules were pushed into the larger CNT from a fluid reservoir held at fixed pressure. Average flow velocities were computed within both CNTs. These velocities were used to calculate a velocity enhancement, defined as the ratio of the downstream fluid velocity to the upstream fluid velocity.

Hanasaki and Nakatani found in their MD simulations that classical fluid mechanics fails dramatically in predicting the velocity enhancement. In particular, the classical approach relates the velocity enhancement to the ratio of cross-sectional areas. However, cross-sectional area ratios based on nominal CNT radii are very inaccurate for predicting velocity enhancement downstream of a constriction.

5.3.2 Improved Analysis using Maximum Accessible Radius

It is only when the excluded volume (due to the stand-off distance between the water and the CNT) is taken into account that the MD simulation results can be explained. Figure 5-8 shows that using Eqn. (3.9) as the basis for a more representative cross-sectional area $\pi r_{\max}^2$ leads to much closer agreement with Hanasaki and Nakatani's MD results. Hanasaki and Nakatani ultimately also recognized that the maximum accessible radius was the most accurate basis for the effective cross-sectional area; however, their values for the maximum accessible radius were only determined empirically.

Figure 5-7: Nanoscale nozzle geometry proposed by Hanasaki and Nakatani, consisting of two CNTs joined at a convergent neck. Figure from [10].

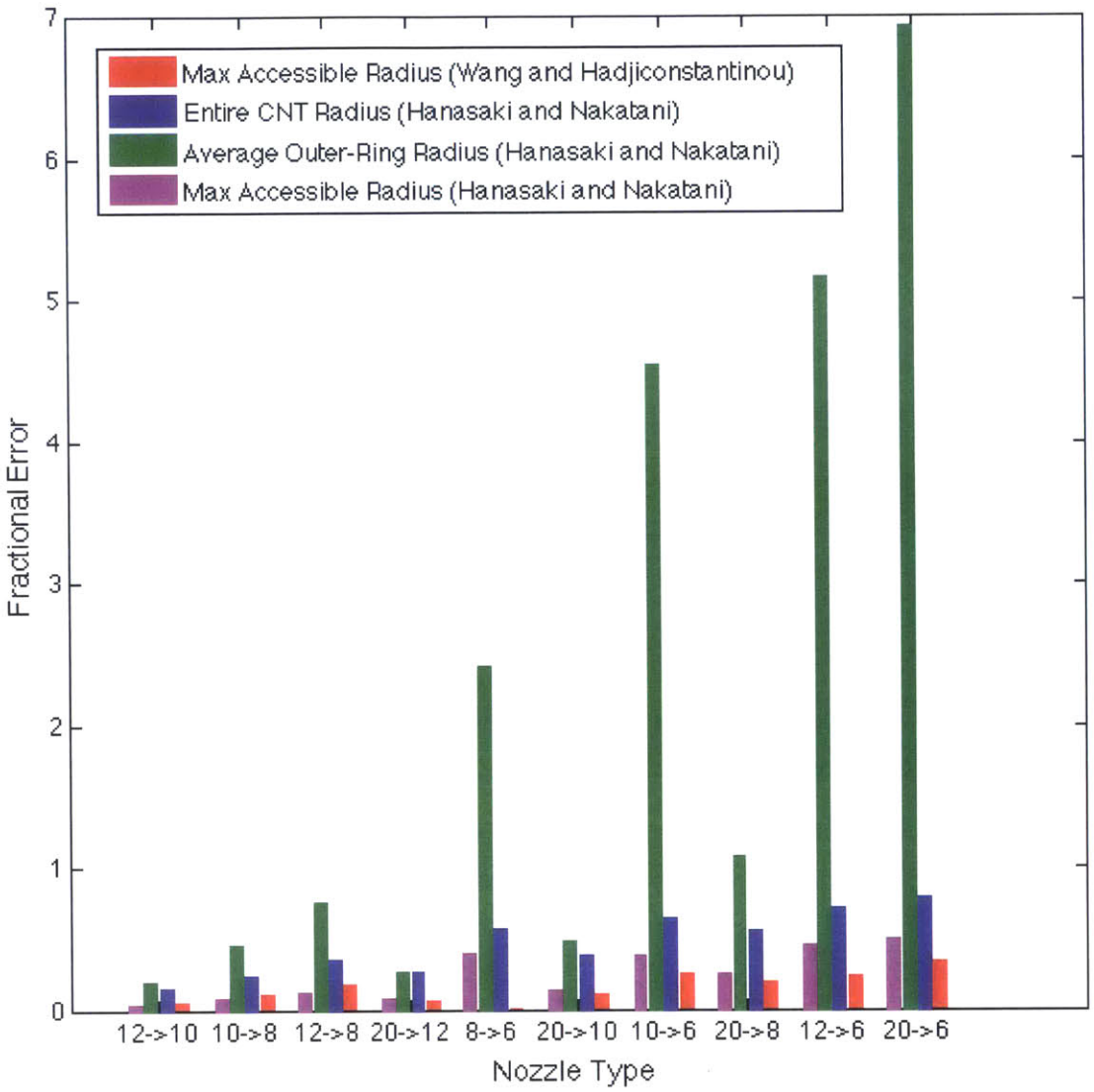

Figure 5-8: Fractional error in predictions of velocity enhancement, defined as $(\chi_{\text{MD}} - \chi_{\text{theory}})/\chi_{\text{MD}}$ where χ refers to the velocity enhancement $\frac{v_{\text{downstream}}}{v_{\text{upstream}}}$, using (3.9) vs. the methods described in Ref. [10]. A nozzle type of the form $m \rightarrow n$ indicates a constriction from an (m, m) CNT to an (n, n) CNT.

Chapter 6

Conclusions and Future Work

"I'm your density... I mean, your destiny!"

– George McFly in *Back to the Future*

6.1 Summary

Fluid densities are low in CNTs (compared to the bulk density) due to the finite range of molecular interactions, which is non-negligible compared to typical CNT radii. The largest contributor to this phenomenon is the excluded volume between the CNT wall and the fluid, whose thickness is on the order of one molecular diameter. As the CNT radius approaches this lengthscale, the area that contains no fluid molecules becomes a large fraction of the total CNT cross-sectional area. For example, for a CNT with $R \approx 10\mathring{A}$, the excluded volume between the wall and the first ring alone accounts for approximately half of the CNT volume. This is the key molecular-scale ingredient underlying the anomalous density phenomenon. In fact, no physically attainable packing within the first ring could possibly yield a first-ring density high enough to make up for this volume deficiency – thus, the density of the nanoconfined fluid will have to be quite low relative to the bulk fluid.

To investigate the anomalous density phenomenon, we have used a mean-field model for fluid-CNT interactions to develop an energetics approach that predicts the structure of fluids confined in CNTs. In particular, this approach yields lengthscales

for the fluid rings and bulk core that form within a CNT. We find that these length-scales agree very closely with results from MD simulations of both LJ fluids and water.

Combining the analytical description of the fluid structure with a characterization of the density in the first two rings from MD simulation provides a closed-form expression for the anomalous density of a confined fluid as a function of CNT radius. This expression is in excellent agreement with MD simulations.

These contributions represent a clear improvement over previous methods used to understand nanoconfined fluid structure and the anomalous density phenomenon. Whereas previous methods relied exclusively on empirical fits to MD simulation results, our model presents new physical insights and accurate quantitative predictions for nanoconfined fluids.

Despite the focus on equilibrium densities, the results discussed here are in some cases already useful for non-equilibrium settings involving fluid flow. For example, our results can be used to estimate the effective cross-sectional area of a CNT, which is vital for accurately predicting the flow velocity enhancement downstream of a constriction.

6.2 Future Directions

The current work suggests several avenues for future investigation. These future directions can be divided into two categories:

1. Improvements to the models presented in Chapter 3.

2. Application of these principles to other nanofluidic systems.

In the case of the former, we first note that the current mean-field approach accounts only for interactions between LJ atoms. Although electrostatic effects between water and carbon are negligible (and so it is possible to use the same mean-field approach to predict the stand-off distance between water and its confining CNT wall), electrostatic effects between water and itself are substantial. Capturing these effects

is important for building a model that quantifies subsequent-ring formation within the outermost fluid ring. After incorporating electrostatic effects, it may be possible to predict the equilibrium nanoconfined density of fluids featuring charged atoms, most notably water. We also note that the expression for predicting the anomalous density presented here (Eqn. (3.17)) still relies on MD simulations to extract the densities of the first two rings. Through more careful statistical mechanical considerations, it may be possible to develop a purely analytical model for these ring densities.

With regard to the latter category, there are numerous potential applications of the concepts developed in this thesis to problems of nanoengineering interest. For example, the energetics approach underlying our models could be used to predict the equilibrium nanoconfined fluid structure for more-complex fluids (e.g. oils or polymers), fluids confined by non-carbon materials (e.g. silica nanopores or boron nitride nanotubes), or fluids confined within non-cylindrical geometries (e.g. conical nanopores). Moreover, we note that non-equilibrium MD simulations have shown that water flow in CNTs does not appreciably affect water structure [8]. Thus information about the equilibrium spatial distribution of density may also prove useful in the development of models that predict water flow rates in CNTs [20], a topic which has attracted considerable attention [11, 12, 13, 14].

Bibliography

[1] Alessio Alexiadis and Stavros Kassinos. The density of water in carbon nanotubes. *Chemical Engineering Science*, 63(8):2047–2056, 2008.

[2] SklogWiki. Spc/e water molecule, 2011.

[3] SklogWiki. Tip4p water molecule, 2011.

[4] R. Saito, M. Fujita, G. Dresselhaus, and M. S. Dresselhaus. Electronic structure of chiral graphene tubules. *Applied Physics Letters*, 60(18):2204–2206, 1992.

[5] M. C. Gordillo and J. Marti. Hydrogen bond structure of liquid water confined in nanotubes. *Chemical Physics Letters*, 329(56):341–345, 2000.

[6] Jun Wang, Yu Zhu, Jian Zhou, and Xiao-Hua Lu. Diameter and helicity effects on static properties of water molecules confined in carbon nanotubes. *Physical Chemistry Chemical Physics*, 6:829–835, 2004.

[7] Yingchun Liu, Qi Wang, Tao Wu, and Li Zhang. Fluid structure and transport properties of water inside carbon nanotubes. *The Journal of Chemical Physics*, 123(23):234701, 2005.

[8] Itsuo Hanasaki and Akihiro Nakatani. Flow structure of water in carbon nanotubes: Poiseuille type or plug-like? *The Journal of Chemical Physics*, 124(14):144708, 2006.

[9] Thomas Werder, Jens H. Walther, Richard L. Jaffe, Timur Halicioglu, Flavio Noca, and Petros Koumoutsakos. Molecular dynamics simulation of contact angles of water droplets in carbon nanotubes. *Nano Letters*, 1(12):697–702, 2001.

[10] Itsuo Hanasaki and Akihiro Nakatani. Water flow through carbon nanotube junctions as molecular convergent nozzles. *Nanotechnology*, 17(11):2794, 2006.

[11] G. Hummer, J. C. Rasaiah, and J. P. Noworyta. Water conduction through the hydrophobic channel of a carbon nanotube. *Nature*, 414:188–190, 2001.

[12] M. Majumder, N. Chopra, R. Andrews, and B. J. Hinds. Nanoscale hydrodynamics: Enhanced flow in carbon nanotubes. *Nature*, 438:44, 2005.

[13] Jason K. Holt, Hyung G. Park, Yinmin Wang, Michael Stadermann, Alexander B. Artyukhin, Costas P. Grigoropoulos, Aleksandr Noy, and Olgica Bakajin. Fast mass transport through sub-2-nanometer carbon nanotubes. *Science*, 312(5776):1034–1037, 2006.

[14] M. Whitby and N. Quirke. Fluid flow in carbon nanotubes and nanopipes. *Nature Nanotechnology*, 2(2):87–94, 2007.

[15] Bruce J. Hinds, Nitin Chopra, Terry Rantell, Rodney Andrews, Vasilis Gavalas, and Leonidas G. Bachas. Aligned multiwalled carbon nanotube membranes. *Science*, 303(5654):62–65, 2004.

[16] Sangjin Park, Youn-Su Kim, Won Bae Kim, and Sangyong Jon. Carbon nanosyringe array as a platform for intracellular delivery. *Nano Letters*, 9(4):1325–1329, 2009.

[17] Sylvain Bernard, Richard Wirth, Anja Schreiber, Hans-Martin Schulz, and Brian Horsfield. Formation of nanoporous pyrobitumen residues during maturation of the barnett shale. *International Journal of Coal Geology*, 103(0):3–11, 2012.

[18] A. Siria, P. Poncharal, A.-L. Biance, R. Fulcrand, X. Blase, S. T. Purcell, and L. Bocquet. Giant osmotic energy conversion measured in a single transmembrane boron nitride nanotube. *Nature*, 494:455–458, 2013.

[19] Theophanes Grammenos and Antonios Giannakopoulos. Fluid ordering effects and density variations in nanochannel flows: a quasicontinuum theory. *Mathematical Methods in the Applied Sciences*, 37(2):200–206, 2014.

[20] Hiromitsu Takaba, Yasushi Onumata, and Shin-ichi Nakao. Molecular simulation of pressure-driven fluid flow in nanoporous membranes. *The Journal of Chemical Physics*, 127(5):054703, 2007.

[21] Ravi Chopra, Thomas M. Truskett, and Jeffrey R. Errington. On the use of excess entropy scaling to describe the dynamic properties of water. *The Journal of Physical Chemistry B*, 114(32):10558–10566, 2010.

[22] W.Q. Wu, H.Y. Chen, and D.Y. Sun. The morphologies of lennard-jones liquid encapsulated by carbon nanotubes. *Physics Letters A*, 377(34):334–337, 2013.

[23] Chandan K. Das and Jayant K. Singh. Melting transition of lennard-jones fluid in cylindrical pores. *The Journal of Chemical Physics*, 140(20):204703, 2014.

[24] Karl P. Travis and Keith E. Gubbins. Poiseuille flow of lennard-jones fluids in narrow slit pores. *The Journal of Chemical Physics*, 112(4):1984–1994, 2000.

[25] Daniel E. Shai, Nathan M. Urban, and Milton W. Cole. Structure and heat capacity of ne and xe adsorbed on a bundle of carbon nanotubes from monte carlo calculations. *Physical Review B*, 77:205427, 2008.

[26] Alessio Alexiadis and Stavros Kassinos. Influence of water model and nanotube rigidity on the density of water in carbon nanotubes. *Chemical Engineering Science*, 63(10):2793–2797, 2008.

[27] K. Koga, G. T. Gao, H. Tanaka, and X. C. Zeng. Formation of ordered ice nanotubes inside carbon nanotubes. *Nature*, 412:802–805, 2001.

[28] Jiaye Su and Hongxia Guo. Control of unidirectional transport of single-file water molecules through carbon nanotubes in an electric field. *ACS Nano*, 5(1):351–359, 2011.

[29] J. A. Thomas and A. J. H. McGaughey. Density, distribution, and orientation of water molecules inside and outside carbon nanotubes. *The Journal of Chemical Physics*, 128(8):084715, 2008.

[30] Bo Peng and Yang-Xin Yu. A density functional theory for lennard-jones fluids in cylindrical pores and its applications to adsorption of nitrogen on mcm-41 materials. *Langmuir*, 24(21):12431–12439, 2008.

[31] Ming Zeng, Yiping Tang, Jianguo Mi, and Chongli Zhong. Improved direct correlation function for density functional theory analysis of pore size distributions. *The Journal of Physical Chemistry C*, 113(40):17428–17436, 2009.

[32] J.-P. Hansen and I. R. McDonald. *Theory of Simple Liquids.* Academic Press, 1990.

[33] Mehran Kardar. *Statistical Physics of Particles.* Cambridge University Press, 2007.

[34] Xiaoning Yang and Xiaopeng Yue. Adsorption and structure of lennardjones model fluid in slit-like amorphous silica nanopores. *Colloids and Surfaces A: Physicochemical and Engineering Aspects*, 301(13):166–173, 2007.

[35] F.R. Hung, K.E. Gubbins, R. Radhakrishnan, K. Szostak, F. Beguin, G. Dudziak, and M. Sliwinska-Bartkowiak. Freezing/melting of lennard-jones fluids in carbon nanotubes. *Applied Physics Letters*, 2005.

[36] Liang-Liang Huang, Qing Shao, Ling-Hong Lu, Xiao-Hua Lu, Lu-Zheng Zhang, Jun Wang, and Shao-yi Jiang. Helicity and temperature effects on static properties of water molecules confined in modified carbon nanotubes. *Physical Chemistry Chemical Physics*, 8:3836–3844, 2006.

[37] Morteza Mohammadi and Masumeh Foroutan. Mixture of ionic liquid and carbon nanotubes: comparative studies of the structural characteristics and dispersion of the aggregated non-bundled and bundled carbon nanotubes. *Physical Chemistry Chemical Physics*, 15:2482–2494, 2013.

[38] Amir Nasrabadi and Masumeh Foroutan. Interactions between polymers and single-walled boron nitride nanotubes: A molecular dynamics simulation approach. *The Journal of Physical Chemistry B*, 114(47):15429–15436, 2010.

[39] Shengli Zhang, Yonghong Zhang, Shiping Huang, Peng Wang, and Huiping Tian. Molecular dynamics simulations of silica nanotube: Structural and vibrational properties under different temperatures. *Chinese Journal of Chemical Physics*, 23(5):497, 2010.

[40] Frank H. Stillinger and Thomas A. Weber. Computer simulation of local order in condensed phases of silicon. *Physical Review B*, 31:5262–5271, 1985.

[41] Loup Verlet. Computer "experiments" on classical fluids. i. thermodynamical properties of lennard-jones molecules. *Physical Review*, 159:98–103, 1967.

[42] Loup Verlet. Computer "experiments" on classical fluids. ii. equilibrium correlation functions. *Physical Review*, 165:201–214, 1968.

[43] Steve Plimpton. Fast parallel algorithms for short-range molecular dynamics. *Journal of Computational Physics*, 117:1–19, 1995.

[44] H. J. C. Berendsen, J. P. M. Postma, W. F. van Gunsteren, A. DiNola, and J. R. Haak. Molecular dynamics with coupling to an external bath. *The Journal of Chemical Physics*, 81(8):3684–3690, 1984.

[45] Shuichi Nosé. A unified formulation of the constant temperature molecular dynamics methods. *The Journal of Chemical Physics*, 81(1):511–519, 1984.

[46] William G. Hoover. Canonical dynamics: Equilibrium phase-space distributions. *Physical Review A*, 31:1695–1697, 1985.

[47] Denis J. Evans and Gary P. Morriss. *Statistical Mechanics of Nonequilibrium Liquids.* Academic Press, 1990.

[48] Jean-Paul Ryckaert, Giovanni Ciccotti, and Herman J.C Berendsen. Numerical integration of the cartesian equations of motion of a system with constraints: molecular dynamics of n-alkanes. *Journal of Computational Physics*, 23(3):327–341, 1977.

[49] Michael P. Allen and Dominic J. Tildesley. *Computer Simulation of Liquids.* Oxford University Press, 1989.

[50] Wendy D. Cornell, Piotr Cieplak, Christopher I. Bayly, Ian R. Gould, Kenneth M. Merz, David M. Ferguson, David C. Spellmeyer, Thomas Fox, James W. Caldwell, and Peter A. Kollman. A second generation force field for the simulation of proteins, nucleic acids, and organic molecules. *Journal of the American Chemical Society*, 117(19):5179–5197, 1995.

[51] William L. Jorgensen and Jeffry D. Madura. Temperature and size dependence for monte carlo simulations of tip4p water. *Molecular Physics*, 56(6):1381–1392, 1985.

[52] H. J. C. Berendsen, J. R. Grigera, and T. P. Straatsma. The missing term in effective pair potentials. *The Journal of Physical Chemistry*, 91(24):6269–6271, 1987.

[53] H. A. Lorentz. Ueber die anwendung des satzes vom virial in der kinetischen theorie der gase. *Annalen der Physik*, 248(1):127–136, 1881.

[54] D. Berthelot. Sur le mélange des gaz. *Comptes Rendus Hebdomadaires des Séances de l'Académie des Sciences*, 126:1703–1855, 1898.

[55] Jianzhong Wu and Zhidong Li. Density-functional theory for complex fluids. *Annual Review of Physical Chemistry*, 58(1):85–112, 2007.

[56] Harry L. Frisch and Joel L. Lebowitz. *Equilibrium Theory of Classical Fluids.* W. A. Benjamin, 1964.

[57] Gaurav Goel, William P. Krekelberg, Mark J. Pond, Jeetain Mittal, Vincent K. Shen, Jeffrey R. Errington, and Thomas M. Truskett. Available states and available space: static properties that predict self-diffusivity of confined fluids. *Journal of Statistical Mechanics: Theory and Experiment*, 2009(4):4006–4019, 2009.

[58] Pablo G. Debenedetti and Thomas M. Truskett. The statistical geometry of voids in liquids. *Fluid Phase Equilibria*, 158160(0):549–556, 1999.

[59] Stephanie Reich, Christian Thomsen, and Janina Maultzsch. *Carbon Nanotubes: Basic Concepts and Physical Properties.* Wiley-VCH, 2004.

[60] George J. Tjatjopoulos, Donald L. Feke, and J. Adin Mann. Molecule-micropore interaction potentials. *The Journal of Physical Chemistry*, 92(13):4006–4007, 1988.

[61] Milton Abramowitz and Irene A. Stegun. *Handbook of Mathematical Functions.* Dover, New York, fifth edition, 1964.

[62] Mark Wilson. The formation of low-dimensional inorganic nanotube crystallites in carbon nanotubes. *The Journal of Chemical Physics*, 124(12):124706, 2006.

[63] Mark Wilson. The dynamic formation of low-dimensional inorganic nanotubes by filling carbon nanotubes. *The Journal of Chemical Physics*, 131(21):214507, 2009.

[64] Jianbing Zhao, Ling Liu, Patricia J. Culligan, and Xi Chen. Thermal effect on the dynamic infiltration of water into single-walled carbon nanotubes. *Physical Review E*, 80:061206, 2009.

[65] William Humphrey, Andrew Dalke, and Klaus Schulten. VMD – Visual Molecular Dynamics. *Journal of Molecular Graphics*, 14:33–38, 1996.

[66] William L. Jorgensen, Jayaraman Chandrasekhar, Jeffry D. Madura, Roger W. Impey, and Michael L. Klein. Comparison of simple potential functions for simulating liquid water. *The Journal of Chemical Physics*, 79(2):926–935, 1983.

[67] Michael W. Mahoney and William L. Jorgensen. A five-site model for liquid water and the reproduction of the density anomaly by rigid, nonpolarizable potential functions. *The Journal of Chemical Physics*, 112(20), 2000.

[68] Hiroki Nada and Jan P. J. M. van der Eerden. An intermolecular potential model for the simulation of ice and water near the melting point. *The Journal of Chemical Physics*, 118(16), 2003.

[69] Jeetain Mittal, Jeffrey R. Errington, and Thomas M. Truskett. Thermodynamics predicts how confinement modifies the dynamics of the equilibrium hard-sphere fluid. *Physical Review Letters*, 96:177804, 2006.

[70] Trond S. Ingebrigtsen, Jeffrey R. Errington, Thomas M. Truskett, and Jeppe C. Dyre. Predicting how nanoconfinement changes the relaxation time of a supercooled liquid. *Physical Review Letters*, 111:235901, 2013.

[71] Ravi Chopra, Thomas M. Truskett, and Jeffrey R. Errington. On the use of excess entropy scaling to describe single-molecule and collective dynamic properties of hydrocarbon isomer fluids. *The Journal of Physical Chemistry B*, 114(49):16487–16493, 2010.

[72] Yury Gogotsi, Joseph A. Libera, Almila G. Yazicioglu, and Constantine M. Megaridis. In-situ fluid experiments in carbon nanotubes. *Materials Research Society Symposium Proceedings*, 633:741–746, 2001.

[73] Shankar Ghosh, A. K. Sood, and N. Kumar. Carbon nanotube flow sensors. *Science*, 299(5609):1042–1044, 2003.